nature COMMUNICATIONS

ARTICLE

https://doi.org/10.1038/s41467-019-13198-y OPEN

Flexible, sticky, and biodegradable wireless device for drug delivery to brain tumors

Jongha Lee[1,2,10], Hye Rim Cho[1,3,10], Gi Doo Cha[1,2,10], Hyunseon Seo[1,2,4], Seunghyun Lee[3], Chul-Kee Park[5], Jin Wook Kim[5], Shutao Qiao[6], Liu Wang[6], Dayoung Kang[1,2], Taegyu Kang[1,2], Tomotsugu Ichikawa[7], Jonghoon Kim[1,2], Hakyong Lee[1,2], Woongchan Lee[1,2], Sanghoek Kim[8], Soon-Tae Lee[9], Nanshu Lu[6], Taeghwan Hyeon[1,2], Seung Hong Choi[1,3*] & Dae-Hyeong Kim[1,2*]

Implantation of biodegradable wafers near the brain surgery site to deliver anti-cancer agents which target residual tumor cells by bypassing the blood-brain barrier has been a promising method for brain tumor treatment. However, further improvement in the prognosis is still necessary. We herein present novel materials and device technologies for drug delivery to brain tumors, i.e., a flexible, sticky, and biodegradable drug-loaded patch integrated with wireless electronics for controlled intracranial drug delivery through mild-thermic actuation. The flexible and bifacially-designed sticky/hydrophobic device allows conformal adhesion on the brain surgery site and provides spatially-controlled and temporarily-extended drug delivery to brain tumors while minimizing unintended drug leakage to the cerebrospinal fluid. Biodegradation of the entire device minimizes potential neurological side-effects. Application of the device to the mouse model confirms tumor volume suppression and improved survival rate. Demonstration in a large animal model (canine model) exhibited its potential for human application.

[1] Center for Nanoparticle Research, Institute for Basic Science (IBS), Seoul 08826, Republic of Korea. [2] School of Chemical and Biological Engineering, Institute of Chemical Processes, Seoul National University, Seoul 08826, Republic of Korea. [3] Department of Radiology, Seoul National University College of Medicine, Seoul 03080, Republic of Korea. [4] Center for Biomaterials, Korea Institute of Science and Technology, Seoul 02792, Republic of Korea. [5] Department of Neurosurgery, Seoul National University College of Medicine, Seoul 03080, Republic of Korea. [6] Center for Mechanics of Solids, Structures and Materials, Department of Aerospace Engineering and Engineering Mechanics, University of Texas at Austin, Austin, TX 78712, USA. [7] Department of Neurological surgery, Okayama University Graduate School of Medicine, Dentistry, and Pharmaceutical Sciences, Okayama 700-8558, Japan. [8] Department of Electronics and Radio Engineering, Kyung Hee University, Gyeonggi 17194, Republic of Korea. [9] Department of Neurology, Seoul National University College of Medicine, Seoul 03080, Republic of Korea. [10] These authors contributed equally: Jongha Lee, Hye Rim Cho, Gi Doo Cha. *email: verocay@snuh.org; dkim98@snu.ac.kr

Treatment of cancers in organs with special blood barriers such as brain, peritoneum, and oculus has always been challenging. Especially, treatment of malignant brain tumors (e.g., glioblastoma; GBM) is extremely difficult[1], because tumor cells survive through surgical resection and radiation therapy[2,3], causing tumor recurrence. Conventional chemotherapies through the intravenous delivery are oftentimes unsuccesful since the blood–brain barrier blocks delivery of drugs to brain tumors[4]. Several researches have improved controlled and targeted drug delivery to brain tumors[5–7]. For example, the biodegradable polymeric wafer[8,9] (Gliadel wafer, Arbor Pharmaceuticals, USA) implanted near the brain surgery site locally delivers drugs to remaining brain tumors and exhibits meaningful improvement. However, further advances in the treatment efficacy are still necessary.

The requirements of the device for the controlled intracranial drug delivery to brain tumors are as follows. The penetration[10] of the released drugs into brain tissues should be high for treatment of infiltrated tumor cells. Local drug delivery to brain tumors without unwanted release to cerebrospinal fluid (CSF) is important[11]. Mechanical mismatch of rigid implantable devices from brain tissues may cause neurological disorders, and thereby soft electronic devices are preferred for intracranial implants[12–14]. Devices with the capability of complete bioresorption can be a good solution to prevent side effects of chronic implants[15–18]. Long-term sustained drug delivery is helpful for cancer treatment[19,20]. Toward accomplishment of these challenging goals altogether, a novel soft biodegradable electronic device that can actuate drug diffusion wirelessly and disappears after a desired period of time[17,21–23] in the brain[15,16] is needed.

Here, we report materials and device technologies for a flexible, sticky, and biodegradable wireless electronic device integrated with a bifacially designed polymer drug reservoir, which is called as a bioresorbable electronic patch (BEP). The BEP, together with an associated mild-thermic actuation protocol, provides long drug diffusion length and drug delivery duration. The flexibility of the oxidized starch (OST)-based patch and its hydrophilic/hydrophobic bifacial design allow conformal adhesion to the target brain tissue[24,25] and enable local and sustained drug delivery, while reducing unintended drug release to CSF. Fully bioresorbable and soft nature of the BEP minimizes potential neurological side effects of rigid intracranial implants[26]. Wireless mild-thermic actuation by the bioresorbable heater with the alternating magnetic field enhances the penetration depth of delivered drugs. The synergetic effect on brain tumor treatment by integration of all these material and device components is confirmed in mouse subcutaneous and canine brain GBM models in vivo.

Results

Overview of materials and devices. The integrated device, BEP, has a bifacial structure that is composed of a hydrophilic drug-loaded OST film and a hydrophobic poly(lactic acid) (PLA) encapsulation film (Fig. 1a). Magnesium-based ultrathin electronic devices, which work as a wireless heater for mild-thermic drug delivery actuation and a wireless temperature sensor for controlled mild-thermic actuation, are embedded in these thin films (Fig. 1b, left). All material elements of the BEP are bioresorbable, and all biodegradation products are materials existing in the human body[27–30] (Fig. 1b, right). The detailed device fabrication process is described in Supplementary Fig. 1. The BEP was packaged (Fig. 1c), sterilized before implantation (Fig. 1d), and applied to animal models for drug delivery to GBM (Fig. 1e, f).

Figure 1e shows the application process of the BEP in a canine GBM model during the craniotomy (Fig. 1e, left) and lamination of the BEP on the surgical site (Fig. 1e, right). The flexible and sticky design of the BEP facilitates its conformal adhesion to the curved brain cavity surface (Fig. 1f). The strong adhesion of the hydrophilic OST bottom drug reservoir is due to the imine conjugation (Fig. 1a, right). These conformal and strong adhesion improves the efficiency of the drug delivery. Meanwhile, the hydrophobic PLA top encapsulation reduces undesirable drug delivery to CSF. The imine conjugation also helps long-term sustained drug delivery. Then, an alternating radio frequency (RF) magnetic field (220 kHz, 360A; Easyheat, Ambrell, USA) is applied to actuate the heater in the BEP wirelessly, which releases drugs from the reservoir, accelerates the intercellular drug diffusion, and enhances the drug penetration depth (Fig. 1f). The alternating RF magnetic field allows long-distance wireless energy transfer through tissues[31], which activates the mild-thermic actuation to promote drug diffusion to microscopic residual tumors invaded in normal brain tissues[32].

Local drug delivery and biocompatibility. We first designed materials for the BEP. It should conformally adhere to the curved brain surface for local drug delivery, for facile heat transfer during mild-thermic actuation, and for prolonged drug delivery duration by minimizing unwanted drug leakage to CSF. This could be achieved by using OST which is synthesized by oxidization of starch (Supplementary Fig. 2). It provides strong imine conjugation to both brain tissues and drug molecules (e.g., doxorubicin; DOX) (Fig. 2a, green), and thus enables good adhesion and sustained drug release. The flexible drug-loaded patch was made by mixing OST with DOX in PBS and dried under the humid condition (Supplementary Fig. 3). DOX was used as a major antitumor agent in this study because of its outstanding therapeutic effect and easy visualization using fluorescence. The maximum DOX loading amount that we have observed was 6.831 mg per one BEP since the DOX is highly miscible to the OST. The total amount of DOX can be increased further by using multiple BEPs. Further optimization to increase the drug loading amount should be done in the future. Temozolomide[33] can also be used as an alternative drug (Supplementary Fig. 3d). The BEP can also deliver multiple anticancer agents (DOX and TMZ) for the combination therapy (Supplementary Fig. 3e). Although we loaded two kinds of drugs in the BEP, the integrity of the device was well maintained.

Since the adhesion force between the OST film and the brain tissue is stronger than the mechanical strength of the brain tissue[34,35], the brain tissue is mechanically torn before the detachment of the film from the brain surface. Therefore, the effect of oxidization of starch on the adhesion strength was indirectly tested on the bovine muscle instead of the brain tissue, since the bovine muscle has higher mechanical strength than the brain tissue. The shear adhesion test (Fig. 2b, inset) of OST exhibited its strong adhesion to the muscle tissues (Fig. 1a, right) than that of unmodified starch film (non-OST case, 0% in Fig. 2b) due to imine conjugation (more oxidized units). The softness of the BEP is optimized for its conformal adhesion to the convoluted brain surface by changing the ratio of OST to glycerol (Supplementary Fig. 4). The strong adhesion and softness enable the conformal contact of the BEP at the tissue surface (Fig. 2c), which allows local drug delivery (Fig. 2c, inset, white circle). The diffusion length by the natural diffusion (Fig. 2c) is small. However, it can be increased by additional mild-thermic actuations.

The drug release from the patch at 37 °C is analyzed for 4 weeks in the phosphate-buffered saline (PBS; Fig. 2d) solution. Compared with unmodified starch, OST shows more sustained drug release, which prolongs the drug delivery duration. The

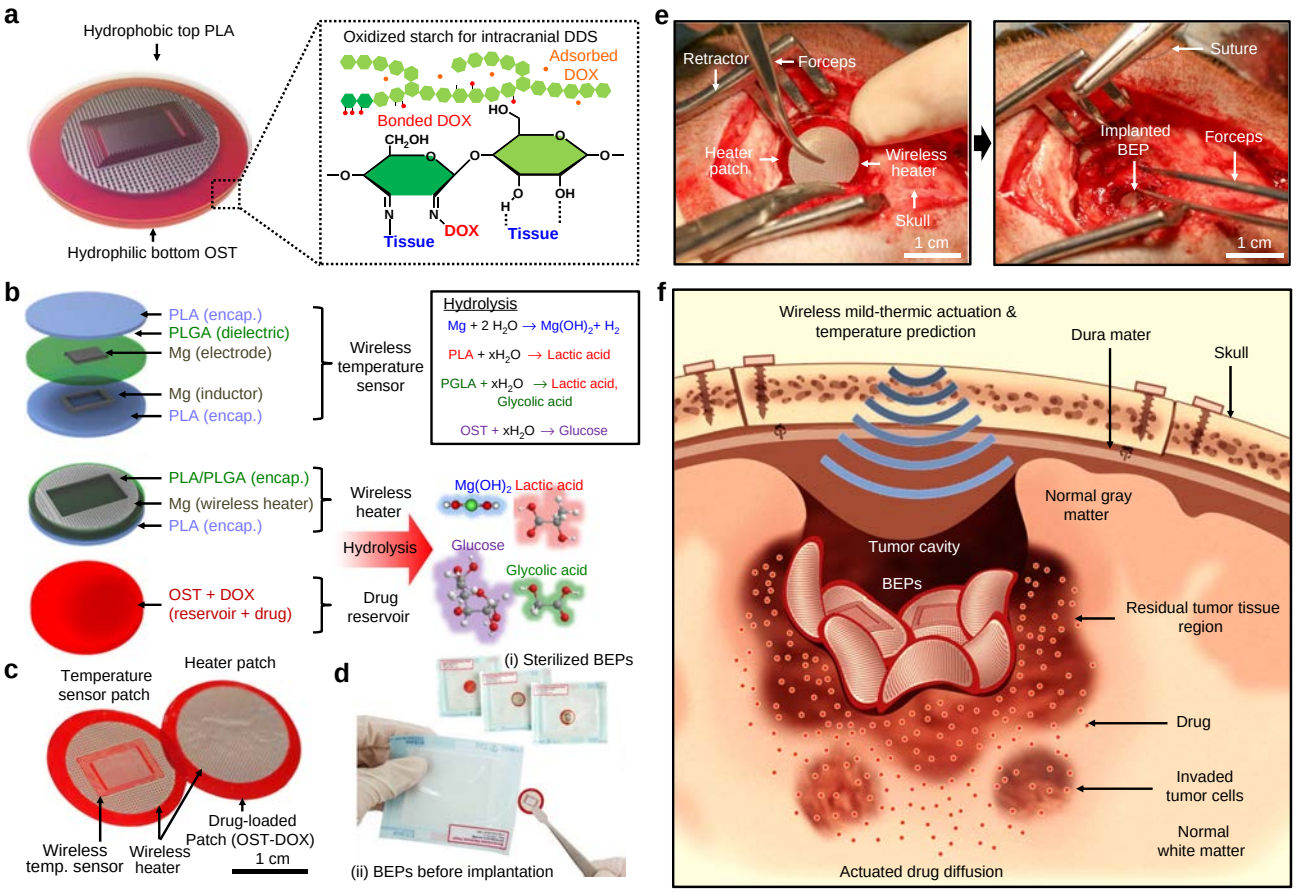

Fig. 1 Materials, device design, and wireless actuation of the bioresorbable electronic patch (BEP). **a** Schematic illustration of the BEP (left) and the molecular structure of drug-containing oxidized starch (OST) (right). **b** Schematic illustration of the BEP and its constituent materials (left), and their biodegradation into hydrolyzed products (right). **c** Image of the BEP, which includes a bioresorbable wireless heater and a temperature sensor on an oxidized starch (OST) patch containing doxorubicin (DOX). **d** Image of the sterilized BEP before implantation. **e** Images of brain craniotomy in the canine model before (left) and after (right) BEP implantation. **f** Schematic illustration of localized and penetrative drug delivery to deep GBM tissues by the BEP with wireless mild-thermic actuation

burst drug release until day 1 (80% of DOX release) in the non-OST case (control) corresponds to release of drugs physically trapped in the polymer chain (Fig. 2a, yellow circle). The suppressed burst release at the early stage (25% DOX until day 1) and the sustained release until later periods (~50% until 4 weeks) can be achieved in OST due to chemical conjugation (i.e., hydrolysis) of drug molecules with polymer chains (Fig. 2a, red circle)[36].

When hydrophobic PLA is coated both on the top and bottom side of the OST substrate, it suppresses the drug release to the PBS solution dramatically (Fig. 2d, red). The selective coating of PLA only on the top surface of the device where the device is exposed to CSF can decrease the unintended drug leakage to other regions (Supplementary Figs. 5, 6; in vitro and in vivo, respectively), although perfect prevention of the drug diffusion to the CSF cannot be achieved due to biodegradation. Meanwhile, the bottom hydrophilic OST substrate enhances adhesion of the BEP to the brain surface and decrease the unintended drug diffusion to CSF (Fig. 2e). The DOX concentration in canine CSF in 1 week after implantation was measured to be 11.9 ng/mL at 3.15 min by high-performance liquid chromatography (HPLC) (Fig. 2f; inset shows HPLC data of DOX standard solutions). This shows minimal DOX leakage to CSF, which is important to prevent drug waste and potential side effects[37].

Fabricating the implant with materials that hydrolyze into components of human body (Fig. 1b)[24] makes the retrieval surgery unecessary[21,38,39] and reduces risks of potential side effects of chronic neural implants[15,16]. Each component of the BEP is converted into biocompatible metabolites. For example, it takes 2 weeks for degradation of the wireless heater (Supplementary Fig. 7a, in vitro degradation; and Supplementary Fig. 7b, in vivo degradation), regardless of the mild-thermic condition (Supplementary Fig. 7c). The biodegradability of the overall device (BEP) was tested in vivo (Fig. 2g). The BEP implanted in canine brain dissolves within 10 weeks without any debris and clinical side effects (Fig. 2g). This 10-week-period corresponds to the entire duration of drug release in vivo.

In order to examine biocompatibility, the BEPs were implanted on the surface of the surgical cavity made by the brain surgery in BALB/c nude mice (Supplementary Fig. 8). The distribution of astrocytes and microglia near the surgical cavity was observed in both the sham (Fig. 2h, i, red) and BEP implantation (Fig. 2h, i, blue) group at various time points (1 day, 2 weeks, 4 weeks, and 6 weeks). No significant increase of the migrated astrocytes and microglia was observed after 2 weeks, and the differences of the migrated astrocytes and microglia between the sham group and the BEP group were not significant overall time periods. The results suggest that the BEP did not induce the significant immune response.

The implantation of the BEP to animals and its mild-thermic actuation in vivo did not affect mouse brain functions. We evaluated whether the BEP can affect the behavior of the mice.

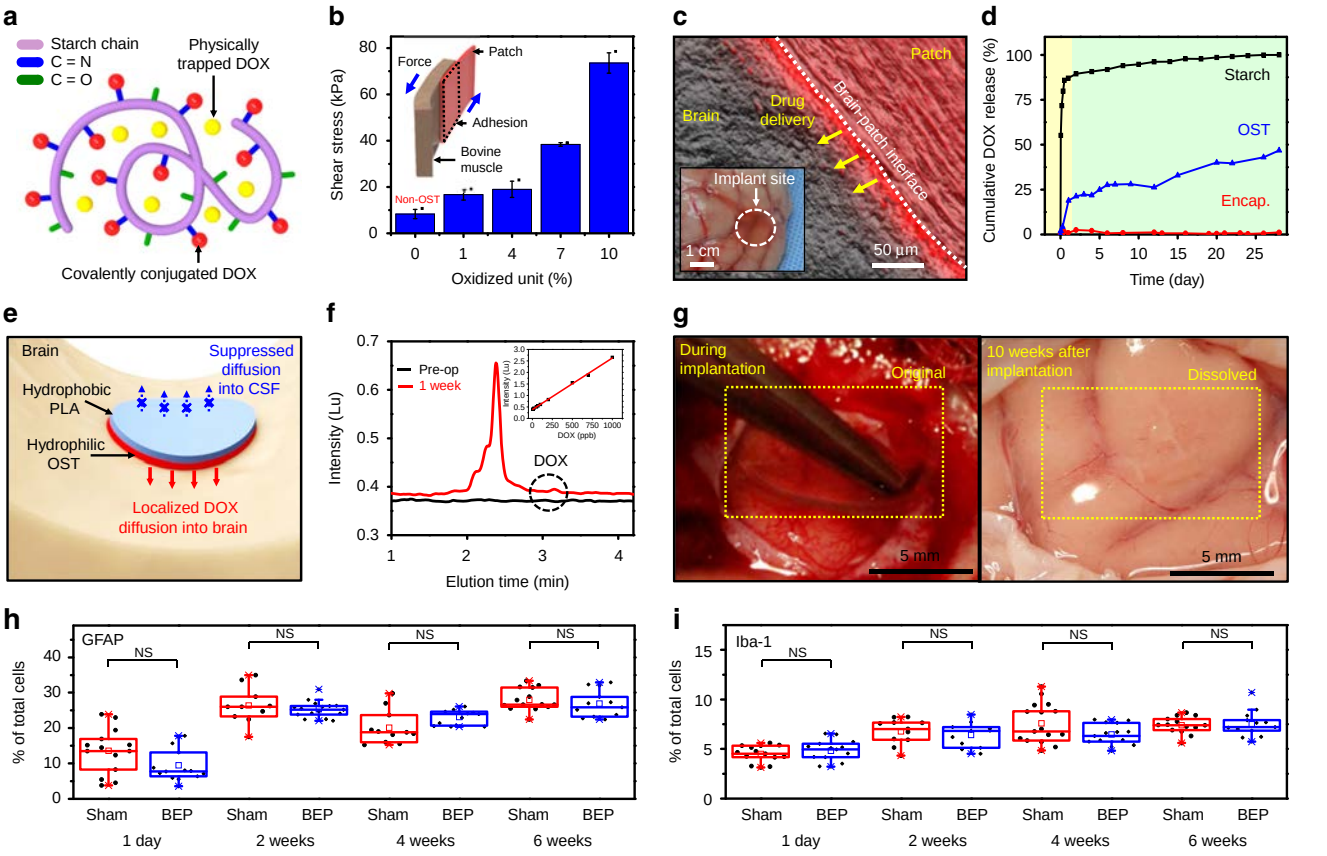

Fig. 2 Materials, device characterization, and biocompatibiltiy. **a** Illustration of the trapped and conjugated DOX to the OST polymer chain. **b** Shear stress for detachment of the OST film with the indicated level of oxidized units from the bovine muscle tissue. Inset shows a schematic illustration of the shear stress measurement. Each experiment was repeated at least three times and error bars represent the standard error of the mean value. **c** Optical microscope image (gray) overlapped by the fluorescence microscope image (red) at the brain-BEP interface. Image of a canine brain after diffusion of DOX from the BEP (inset). **d** Cumulative release of DOX from unmodified starch (black), OST (blue), and PLA-encapsulated OST (red) in 37 °C phosphate-buffered saline (PBS) solution for 4 weeks. **e** Illustration of the flexible bifacial patch conformally adhered on the brain cavity surface. **f** Measurement of DOX concentration (dotted circle) in cerebrospinal fluid (CSF) after 1 week from implantation by HPLC. Inset shows HPLC measurement of standard DOX solutions. **g** Optical camera image during the intracranial BEP implantation surgery (left) and at 10 weeks after implantation (right). Quantification of the immunohistochemistry using BALB/c nude mice at different time points for the sham (red) and BEP implantation (blue) group ($n = 7$–8 for each group and time): **h** for GFAP and **i** for Iba-1. (NS; $p > 0.05$ by paired t-test). Line: median box: 25th–75th percentiles, Whisker: min to max, $^*p < 0.05$ by Man–Whitney U-test with Bonferroni correction

The behavior was evaluated by the rotarod test (Supplementary Fig. 9a, b). The intracranial electroencephalogram was also monitored and analyzed (Supplementary Fig. 9c). According to the mouse tests, no neurological deficits and abnormal behaviors were observed.

The biocompatibility of the BEP was also tested in a large animal (canine model). The BEP contains MRI contrast agents, ferrimagnetic iron oxide nanocubes[40] (Supplementary Fig. 10), and thus its bioresorption and shape change in brain can be monitored by MRI in vivo (Supplementary Fig. 11). The MR images at different time points showed that the conformal contact of the BEP to the brain surface was maintained during its degradation. Compared with its initial state, the patch volume decreased significantly after 9 weeks due to its bioresorption (Supplementary Fig. 12a). Also, the intracranial implantation of the BEP to canine brain did not exhibit any unexpected side effects including brain swelling (Supplementary Fig. 11). The brain tissue reaction to the BEP was evaluated by immunochemical staining using hematoxylin and eosin (H&E) and macrophage antibody in 1 week and 10 weeks after implantation. Any significant inflammatory responses or physiological complications were not observed (Supplementary Fig. 12b). The longer-term studies to observe the effect of hydrolyzed materials in vivo are needed in the future.

Wireless mild-thermic actuation for accelerated drug delivery. The acceleration of drug release by wireless mild-thermic actuation (Fig. 3a) was characterized. The RF magnetic field applied by an external coil triggers eddy current and joule heating in the heater of the implanted BEP (Fig. 3b), resulting in the increased temperature of the BEP and surrounding brain tissues. Key parameters of the heater design are the diameter and thickness of the round-shaped heater while the transmission coil current and coil-to-heater distance can be varied to optimize the heat generation. The hole array in the wireless heater is helpful for facile fabrication (transfer printing) of the device but slightly affects the heat generation (Supplementary Fig. 13a, b). The temperature change under the various coil-to-heater distances in the heater (Fig. 3c) of different diameters and under the various coil-currents in 12 mm diameter heater (Fig. 3c, inset) were measured using our instrument to set the temperature change. Under different conditions, the calibration curve that shows the temperature increase as a function of the magnetic field (Supplementary Fig. 13c) and/or the total eddy current (Supplementary Fig. 13d)

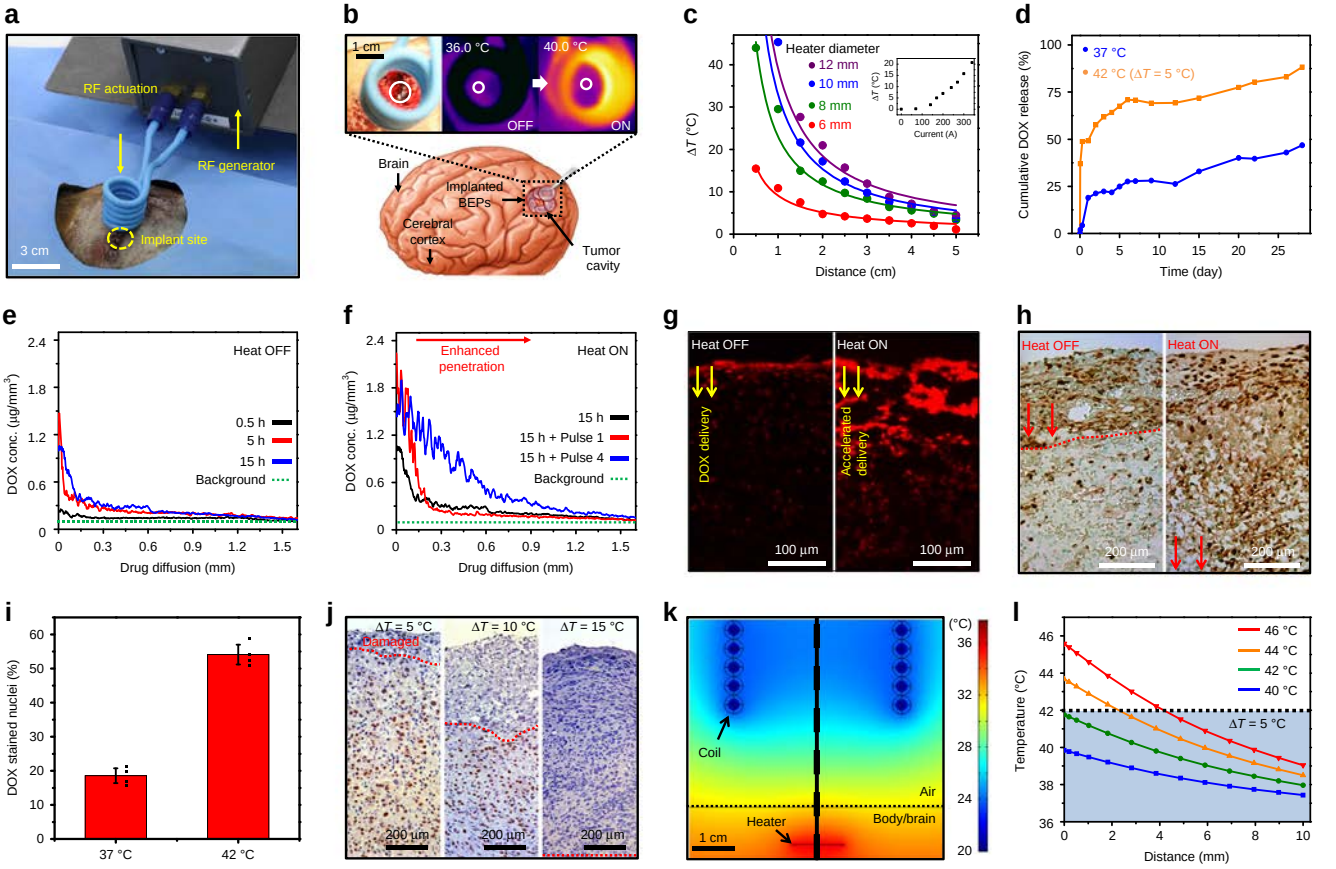

Fig. 3 Wireless mild-thermic drug delivery. **a** Image of radio frequency (RF) wireless mild-thermic actuation in the canine GBM model. **b** Schematic illustration of implanted BEPs and images of the mild-thermic actuation: optical (left) and infrared camera images before (middle) and during (right) the wireless mild-thermic actuation. **c** Experimentally measured temperature change of the BEP by wireless heating depending on the coil-to-heater distance. The inset shows the temperature change depending on the induced current. **d** Cumulative release of DOX from OST in PBS at 37 °C (blue) and 42 °C (orange) for 4 weeks. **e** In vivo measurement of the DOX concentration at the indicated time points after implantation of the BEP without mild-thermic actuation. **f** In vivo measurement of the DOX concentration at 15 h after implantation of the BEP with the pulsed mild-thermic actuation; control (black; no pulse), 1 pulse (red), or 4 pulses (blue). **g** Fluorescence microscope images after 15 h implantation, which show DOX diffusion from the BEP into U87-MG tumor tissues in the mouse model in vivo without (left) and with (right) the mild-thermic actuation. **h** Terminal deoxynucleotidyl transferase dUTP nick end labeling (TUNEL) assay of U87-MG tumor tissues without (left) and with (right) the mild-thermic actuation. **i** Proportion of DOX-stained cells after exposure to the DOX solution for 1 h at 37 and 42 °C, measured by flow cytometry. Each experiment was repeated at least four times and error bars represent the standard error of the mean value. **j** Effect of elevated temperatures on U87-MG tumor tissues, observed by survivin expression. **k** Contour plot of the temperature distribution during the mild-thermic actuation. **l** Simulated temperature profile from the BEP surface into the brain under various heater temperatures. The shadowed part represents the temperature that can be tolerated by the brain tissue

can be used to optimize the amount of heating. Also, the dimension of the heaters (thickness and diameter) can be decreased or the coil-to-heater distance can be increased further by controlling the instrumental parameters such as the RF frequency (Supplementary Fig. 13e, f). More details are described in Supplementary Methods 1.1.

The amount of the drug release can be increased by mild-thermic actuation at 42 °C ($\Delta T = 5$ °C; Fig. 3d). The concentration gradient of DOX delivered into human GBM tissues (U87-MG) with and without mild-thermic actuation was quantified in an immune-deficient mouse in vivo by integrating equidistant fluorescent signal counts. The natural diffusion of DOX (Fig. 3e) is similar to the natural diffusion of carmustine[41,42], and the mild-thermic actuation dramatically enhances drug diffusion (Fig. 3f, g). The actuation condition of $\Delta T = 5$ °C (30 min of 2 pulses) results in death of deep cancer cells, which is shown in the cross-sectional tissue staining image by terminal deoxynucleotidyl transferase dUTP nick end labeling (TUNEL) assay (Fig. 3h). The drug delivery based on mild-thermic actuation over the longer period of time (42 °C, 2 days, ex vivo) results in the enhanced drug delivery depth (~11 mm, Supplementary Figs. 14 and 15a), where the drug concentration is over CC50 of the tumor cell (0.15 μg/mL; Supplementary Fig. 15b). This increased drug penetration is due to increased cell membrane permeability[43] at increased temperature. The U87-MG cell is exposed to the drug solution (DOX of 0.2 μg/mL) at 37 °C and 42 °C for 1 h, and the number of nuclei stained by DOX is measured to compare drug diffusion. The three-times higher drug uptake is observed at the higher temperature (Fig. 3i and Supplementary Fig. 16).

The appropriate level of mild-thermic actuation promotes the drug diffusion while minimizing the thermal damage to surrounding brain tissues[44], but excessive hyperthermia may cause apoptosis[45] of normal brain tissues. Thermal damage to the brain tissue is analyzed by detecting expression of apoptosis inhibitors with survivin (Fig. 3j and Supplementary Fig. 17). The temperature increase of 5 °C for 30 min induced minimal apoptosis, while the temperature increase of 10 or 15 °C caused significant cell death (Fig. 3j). Numerical simulations (Fig. 3k, Supplementary Fig. 18 and Supplementary Table 3) also indicate that no excessive heat is applied to the brain tissue

under $\Delta T = 5$ °C, which is consistent with experiments (Fig. 3j). Heat is dissipated by blood flow at distal regions (Fig. 3k). The absence or presence of skull does not cause differences on temperature distribution according to 3D modeling (Supplementary Fig. 19 and Supplementary Table 4). The details of thermal modeling are described in Supplementary Methods 1.2. Although we tried to maintain the target temperature to be stable as shown in Fig. 3b experiments and Fig. 3k simulations, it is true that temperature fluctuations happen under pulsed wireless thermal actuations in vivo. More reliable and elaborate heating protocols should be developed through large scale in vivo animal experiments in the future.

The optimal coil-to-heater distance at a given heater radius, in which temperature is below 42 °C, can be estimated through simulations (Fig. 3l). The drug diffusion coefficient increases significantly by wireless mild-thermic actuation of $\Delta T = 5$ °C, consistent with previous reports (Supplementary Fig. 18a[43,46]). For experimental validation of the optimal distance, temperature increase by mild-thermic actuation is estimated by either an IR camera or a wireless temperature sensor of the BEP (Supplementary Fig. 20 and Supplementary Methods 1.3). The optimum actuation condition is adopted to the therapy protocol.

Evaluation of therapeutic efficacy in the mouse and canine GBM model. We evaluated therapeutic efficacy of the BEP in vivo by using the human xenograft GBM model with immune-deficient mice (BALB/c nude mice). Human GBM cells (U87-MG) were cultured and subcutaneously implanted near the thigh region of 6-week-old nude mice ($n = 33$). Tumor was grown and resected similar to the standard protocol of human brain tumor[47] therapy, and then the BEP of ~14 mm diameter was implanted. Detailed surgical procedures are provided in Supplementary Methods 1.4 and Supplementary Fig. 21. The protocol for the therapy is presented in Fig. 4a. The procedure starts from the tumor resection. Further studies for the nonresectable tumor cases are also needed in the future.

Mice were divided into five groups: each treated with (1) intravenous injection of DOX (IV group, Supplementary Fig. 22a); (2) implantation of the BEP without DOX but with mild-thermic actuation (Heating group; Supplementary Fig. 22b); (3) implantation of the BEP with DOX but without heating (OST group; Supplementary Fig. 22c); (4) implantation of the custom-made control wafer of which the composition is same as the Gliadel wafer (194.4 mg poly[bis(p-carboxyphenoxy)propane] anhydride and sebacic acid containing 7.7 mg carmustine) (control wafer group; Fig. 4b); and (5) implantation of the BEP with DOX and with mild-thermic actuation (OST + Heating group; Fig. 4c). The DOX concentration in the BEP is 0.69 mg/BEP. The Heating and OST + Heating group received wireless mild-thermic treatment for 2 weeks following the therapy protocol (Fig. 4a).

The IV and Heating group exhibited poor prognoses, while the OST and control wafer group showed meaningful suppression of tumor recurrence (Supplementary Table 1). In particular, the OST + Heating group exhibited significantly reduced tumor volume among all groups, even compared with the control wafer group ($p = 0.0048$) as shown in Fig. 4d and Supplementary Table 1. It also leads to the dramatic increase in the survival rate among all groups, even compared with the control wafer group ($p = 0.013$) as shown in Fig. 4e and Supplementary Table 2. This improvement in therapeutic efficacy shows combined benefits of local drug delivery to the target region, long-lasting therapy due to sustained drug release, and enhanced drug penetration by mild-thermic actuation. Since the microenvironment in thigh is different from that in brain, we additionally established a mouse brain tumor model to prove efficacy of mild-thermic actuation in brain (Supplementary Fig. 23a–e), which exhibited consistent results with the subcutaneous tumor model results (Supplementary Fig. 23 and Supplementary Methods 1.5).

To obtain preclinical data of the BEP in large animals, a canine GBM model was established. Since canine brain is much larger than mouse brain, it allows a similar procedure with standard human GBM surgery (Supplementary Fig. 24). Detailed procedures are described in Supplementary Methods 1.6. Similar to the conventional neurosurgery, the implanted GBM tissues were partially removed by surgery while residual infiltrative tumor tissues remained in the surgical cavity (Fig. 4f). The BEP was implanted to the cavity, and the surgical site was covered by surgical glue and skin without skull. Supplementary Fig. 25 shows that tissues near the cavity have little mechanical damages, confirming the surgical process is successful. The tumor volume continuously increased unless treated (Fig. 4g, left). When wireless mild-thermic treatment ($\Delta T = 5$ °C, 30 min; 2 pulses) was applied by the BEP, however, tumor growth was suppressed (Fig. 4g, right) by intracranial drug delivery (Fig. 4h).

To evaluate therapeutic effect of the BEP further, both the BEP and a control wafer were implanted to the brain cavity with the remaining brain tumor in two different mongrel dogs. The treatment with the BEP and the control wafer for 2 days caused apoptosis of tumor cells, which are confirmed by TUNEL assay (Fig. 4i, j and Supplementary Fig. 26). Both cases showed apoptosis of tumor cells within 2 mm from the cavity surface. However, the BEP induced apoptosis of deeply invaded microscopic tumor cells (Fig. 4i) at 5 mm (Fig. 4j, Magnified H&E TUNEL images in Supplementary Fig. 26a, b), while the control wafer could not treat tumor cells located over 2 mm depth from the cavity surface (Supplementary Fig. 26c, d). More deeply seated tumor cells could be treated by the BEP, since drug penetration can be extended by mild-thermic actuation of the BEP.

Discussion

In conclusion, we have developed a flexible, sticky, and biodegradable wireless device using bioresorbable materials and electronics design. The device, together with an associated mild-thermic drug delivery protocol, achieved enhanced therapeutic efficacy in brain tumor treatment. The integrated device and protocol offered wirelessly controlled, spatially focused, and temporally extended delivery of antitumor agents up to deeply located brain tumors. The BEP dramatically suppressed tumor volume and enhanced survival rate in vivo. The fully bioresorbable nature of the BEP provided intracranial biocompatibility and minimized potential side effects. The proposed material and device technology represents an important step toward intracranial treatment of brain tumors.

Methods

Fabrication of the BEP. A sacrificial layer of poly(methyl methacrylate) (PMMA; A11, Microchem, USA) was spin coated (176 g, 30 s) onto a silicon wafer and cured at 180 °C for 3 min. The diluted polyimide (PI) precursor solution (poly(pyromellitic dianhydride-co-4,4′-oxydianiline), amic acid solution; Sigma Aldrich, USA) was spin coated onto the substrate (176 g, 60 s) and cured at 250 °C for 2 h to form a bottom PI layer. PI was diluted by mixing the same mass of the PI precursor solution and 1-methyl-2-pyrrolidinone (Sigma Aldrich, USA). A ZnO thin film (2 nm) was deposited by AC sputtering under an Ar atmosphere (5 mTorr, 30 W) as an adhesion layer. In sequence, 3 μm of magnesium was deposited using a thermal evaporator. Then, AZ5214 photoresist (PR; Microchem, USA) was spin coated and patterned. The magnesium was etched using a custom-made magnesium etchant (nitric acid:deionized water:ethylene glycol; 1:1:3) to pattern the wireless heater and temperature sensor. The diluted PI precursor solution was again spin coated onto the substrate (176 g, 60 s) and cured at 250 °C for 2 h to form a top PI layer. Then, the top and bottom PI layers were patterned using AZ4620 PR (Microchem, USA). The PI was etched by oxygen plasma using a reactive-ion etcher (O_2, 100 sccm, 0.1 Torr, 100 W). After patterning the PI, the sacrificial PMMA layer was undercut etched using acetone at 70 °C. The device, delaminated from the substrate, was picked up using a polydimethylsiloxane

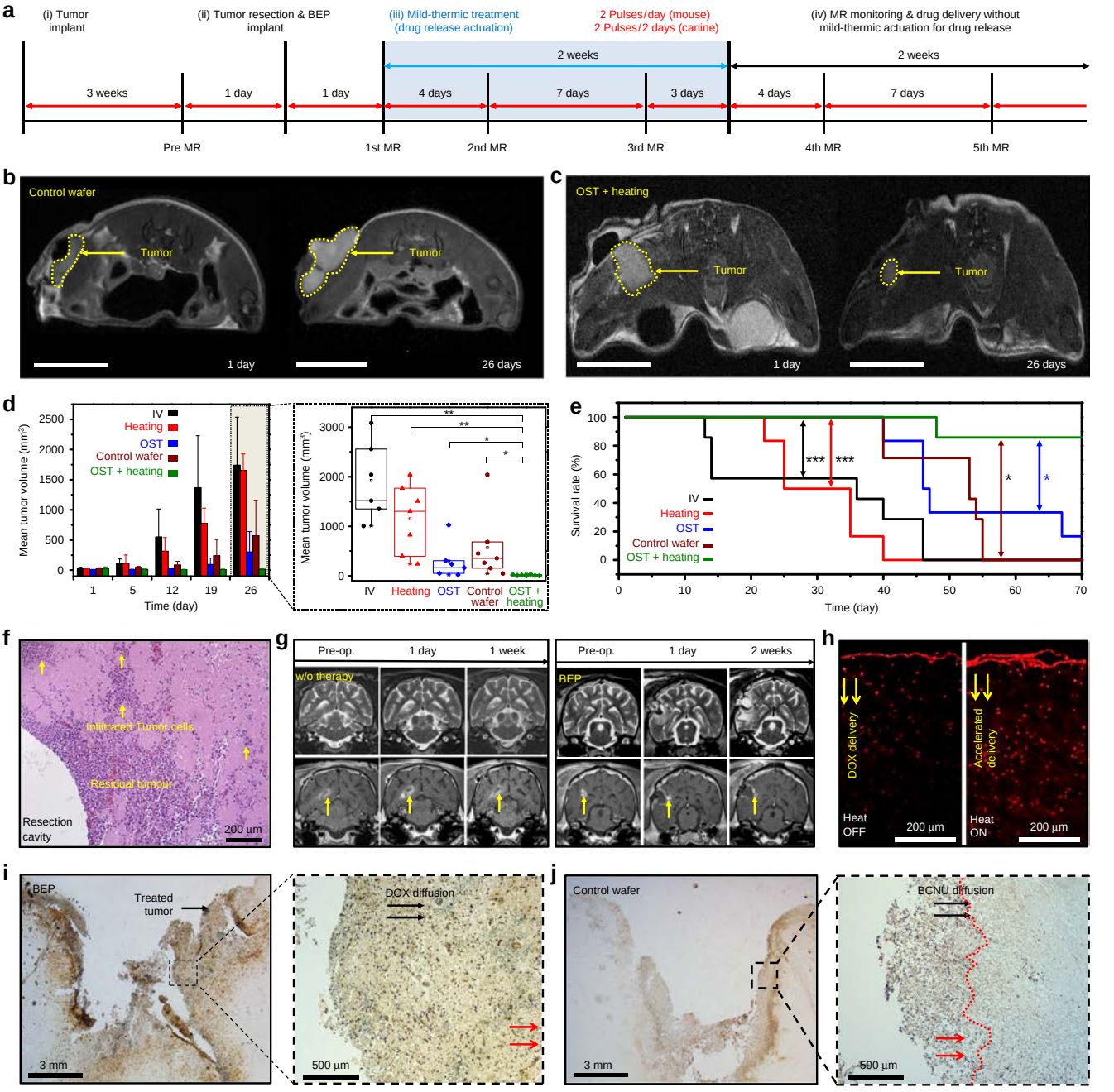

Fig. 4 Therapeutic efficacy of the BEP in BALB/c nude mouse and canine brain tumor models. **a** Therapy protocol employed to investigate the BEP in both mouse and canine model. **b** Representative axial T2-weighted MR images of the control wafer group, and **c** OST + Heating group at the indicated time points after surgery in the mouse model. **d** Time dependent mean tumor volumes of the indicated groups (left) and box-and-whisker plots of tumor volumes at 26 days after surgery (right). $n = 6, 7, 6, 7, 6$ for IV, Heating, OST, OST + Heating, and control wafer group, respectively in the mouse model. Line: median Box: 25th–75th percentiles, Whisker: min to max, $^{*}p < 0.05$, $^{**}p < 0.01$ by Man–Whitney *U*-test with Bonferroni correction. **e** Kaplan–Meier survival rate plots of the indicated treatment group in the mouse model, $^{*}p < 0.05$ by log-rank test with Bonferroni correction. **f** Histology images of tissues near the J3T-1 implantation site stained with H&E in the canine model. **g** Coronal T2- (top) and contrast-enhanced T1-weighted MR images of the tumor without (left) and with (right) the BEP treatment in the canine model. **h** Fluorescence images of DOX diffused from the BEP into the J3T-1 tissue in the canine model in vivo without (left) and with the mild-thermic actuation in the canine model. **i** TUNEL assay of the BEP treatment case after 2 days from the implantation (left) and its magnified view (right) in the canine model. **j** TUNEL assay of the control wafer treatment case after 2 days from the implantation (left) and its magnified view (right) in the canine model

(PDMS) stamp (Sylgard 184, A:B = 10:1). Then, the bottom PI layer was etched by oxygen plasma. Separately, 3% (*w*/*w*) PLA or 8% (*w*/*w*) PLGA was spin coated on top of the OST film several times. The patch was exposed to the vapor of boiling chloroform to make the PLA or PLGA sticky prior to transferring the device from the PDMS stamp to the OST film. After the transfer, the top PI layer was etched by oxygen plasma. Finally, PLA and PLGA were spin coated several times for top encapsulation to protect the magnesium-based electronic device. Before implantation of the BEP, each device that was transferred onto the OST film was cut to have a circular shape with the diameter of 14 mm.

Mild-thermic actuation procedure. The mild-thermic actuation was applied under the anesthesia in both mouse and canine model without the skull but with the cover of the surgical glue and skin. The heating procedure consists of 30 min

pulse for two times every day in the mouse model, and 30 min pulse for two times every 2 days in the canine model to prevent anesthetic death.

Histology. Tissues were fixed in 10% formalin, incubated in graded ethanol, embedded in paraffin, and cut into 4-μm-thick sections. The histological analyses were performed with H&E staining for basic morphological evaluation and TUNEL (terminal deoxynucleotidyl transferase dUTP nick end labeling) staining for apoptotic cell detection. For immunohistochemistry (IHC), all tissue sections were deparaffinized in xylene and hydrated by immersion in a graded ethanol series. Antigen retrieval was performed in a microwave by placing the sections in epitope retrieval solution (0.01 M citrate buffer, pH 6.0) for 20 min; endogenous peroxidase was inhibited by immersing the sections in 0.3% hydrogen peroxide for 10 min. The sections were then incubated with a primary mouse monoclonal antibody to macrophage (ThermoFisher Scientific, USA, MAC387, dilution 1:200) for inflammatory macrophages in a canine model or a rabbit monoclonal antibody to survivin (Cell Signaling, USA, #2808, dilution 1:300) in Dako REAL antibody diluent (Dako, USA) for a mouse model. The IHC staining of GFAP and Iba-1 for biocompatibility test was performed with the rabbit monoclonal anti-GFAP (Abcam, USA, ab7260, dilution 1:2000) and anti-Iba-1 (Wako Chemicals, USA, 019–19741, dilution 1:3000) using the Dako Autostainer Link 48 system according to recommended protocols. Two regions of interest from each slide were acquired and all images were analyzed using Image J.

Statistics. The final tumor volume for all mice in each group was compared and evaluated by using the Mann–Whitney *U*-test. The *p* value for the individual test was multiplied by the number of comparison made (Bonferroni correction). The log-rank test was used to compare the survival plot of each group. The *p* value for the individual test was also multiplied by the number of comparison made (Bonferroni correction). The paired *t*-test was used to compare the rotarod retention time of two groups. The paired *t*-test was used to compare the quantification results of immunohistochemistry.

Ethical approval. This study was approved by our Institutional Animal Care and Use Committee (IACUC; No. 14-0156-C2A3) and was performed in accordance with our IACUC guidelines and with the National Institute of Health Guide for the Care and Use of Laboratory Animals.

Cell lines. The human GBM cell line (U87-MG) was obtained from the American Type Culture Collection (Rockville, USA, HTB-14) and maintained in RPMI medium with 10% fetal bovine serum (FBS) at 37 °C. All cell lines were routinely tested to exclude infection with mycoplasma and reauthenticated using microsatellite profiling immediately prior to manuscript submission. The canine glioblastoma cell line (J3T-1), which was derived from the parental canine glioma cell line (J3T), was provided by T.I, Okayama University Graduate School of Medicine, Dentistry, and Pharmaceutical Sciences (Japan) after obtaining research ethics approval, and maintained in the Roswell Park Memorial Institute (RPMI) medium with 10% FBS at 37 °C[48–50]. For this study, the cell line used was routinely tested to exclude infection with mycoplasma.

Reporting summary. Further information on research design is available in the Nature Research Reporting Summary linked to this article.

Data availability

The datasets generated during and/or analysed during the current study are available from the corresponding author upon reasonable request.

Received: 9 April 2019; Accepted: 21 October 2019;
Published online: 15 November 2019

References

1. Krex, D. et al. Long-term survival with glioblastoma multiforme. *Brain*. **130**, 2596–2606 (2007).
2. Stupp, R. et al. Effects of radiotherapy with concomitant and adjuvant temozolomide versus radiotherapy alone on survival in glioblastoma in a randomised phase III study: 5-year analysis of the EORTC-NCIC trial. *Lancet Oncol.* **10**, 459–466 (2009).
3. Lawrence, Y. R. et al. Radiation dose-volume effects in the brain. *Int. J. Rad. Oncol. Biol. Phys.* **76**, S20–S27 (2010).
4. Lesniak, M. S. & Brem, H. Targeted therapy for brain tumours. *Nat. Rev. Drug Discov.* **3**, 499–508 (2004).
5. Upadhyay, U. M. et al. Intracranial microcapsule chemotherapy delivery for the localized treatment of rodent metastatic breast adenocarcinoma in the brain. *Proc. Natl Acad. Sci.* **111**, 16071–16076 (2014).
6. Sun, T. et al. Closed-loop control of targeted ultrasound drug delivery across the blood–brain/tumor barriers in a rat glioma model. *Proc. Natl Acad. Sci. USA*. **114**, E10281–E10290 (2017).
7. Jain, A. et al. Guiding intracortical brain tumour cells to an extracortical cytotoxic hydrogel using aligned polymeric nanofibres. *Nat. Mater.* **13**, 308–316 (2014).
8. Xing, W.-k, Shao, C., Qi, Z.-y, Yang, C. & Wang, Z. The role of Gliadel wafers in the treatment of newly diagnosed GBM: a meta-analysis. *Drug. Des. Dev. Ther.* **9**, 3341–3348 (2015).
9. Chowdhary, S. A., Ryken, T. & Newton, H. B. Survival outcomes and safety of carmustine wafers in the treatment of high-grade gliomas: a meta-analysis. *J. Neurooncol.* **122**, 367–382 (2015).
10. Fung, L. K. et al. Pharmacokinetics of interstitial delivery of carmustine, 4-hydroperoxycyclophosphamide, and paclitaxel from a biodegradable polymer implant in the monkey brain. *Cancer Res.* **58**, 672–684 (1998).
11. Bota, D. A., Desjardins, A., Quinn, J. A., Affronti, M. L. & Friedman, H. S. Interstitial chemotherapy with biodegradable BCNU (Gliadel) wafers in the treatment of malignant gliomas. *Ther. Clin. Risk. Manag.* **3**, 707–715 (2007).
12. Zhou, T. et al. Syringe-injectable mesh electronics integrate seamlessly with minimal chronic immune response in the brain. *Proc. Natl Acad. Sci. USA*. **114**, 5894–5899 (2017).
13. Fu, T.-M. et al. Stable long-term chronic brain mapping at the single-neuron level. *Nat. Methods* **13**, 875–882 (2016).
14. Park, S. et al. One-step optogenetics with multifunctional flexible polymer fibers. *Nat. Neurosci.* **20**, 612–619 (2017).
15. Yu, K. J. et al. Bioresorbable silicon electronics for transient spatiotemporal mapping of electrical activity from the cerebral cortex. *Nat. Mater.* **15**, 782–791 (2016).
16. Kang, S.-K. et al. Bioresorbable silicon electronic sensors for the brain. *Nature* **530**, 71–76 (2016).
17. Shin, J. et al. Bioresorbable pressure sensors protected with thermally grown silicon dioxide for the monitoring of chronic diseases and healing processes. *Nat. Biomed. Eng.* **3**, 37–46 (2019).
18. Boutry, C. M. et al. Biodegradable and flexible arterial-pulse sensor for the wireless monitoring of blood flow. *Nat. Biomed. Eng.* **3**, 47–57 (2019).
19. Zhang, R. X. et al. Design of nanocarriers for nanoscale drug delivery to enhance cancer treatment using hybrid polymer and lipid building blocks. *Nanoscale*. **9**, 1334–1355 (2017).
20. Zhao, M. et al. Post-resection treatment of glioblastoma with an injectable nanomedicine-loaded photopolymerizable hydrogel induces long-term survival. *Int. J. Pharm.* **548**, 522–529 (2018).
21. Hwang, S.-W. et al. A physically transient form of silicon electronics. *Science*. **337**, 1640–1644 (2012).
22. Tao, H. et al. Silk-based resorbable electronic devices for remotely controlled therapy and in vivo infection abatement. *Pro. Natl Acad. Sci. USA*. **111**, 17385–17389 (2014).
23. Koo, J. et al. Wireless bioresorbable electronic system enables sustained nonpharmacological neuroregenerative therapy. *Nat. Med.* **24**, 1830–1836 (2018).
24. Hwang, S.-W. et al. 25th Anniversary article: Materials for high-performance biodegradable semiconductor devices. *Adv. Mater.* **26**, 1992–2000 (2014).
25. Choi, S. et al. Highly conductive, stretchable and biocompatible Ag–Au core–sheath nanowire composite for wearable and implantable bioelectronics. *Nat. Nanotechnol.* **13**, 1048–1056 (2018).
26. Lacour, S. P., Courtine, G. & Guck, J. Materials and technologies for soft implantable neuroprostheses. *Nat. Rev. Mater.* **1**, 16063 (2016).
27. Zheng, Y. F., Gu, X. N. & Witte, F. Biodegradable metals. *Mater. Sci. Eng. R.* **77**, 1–34 (2014).
28. Nair, L. S. & Laurencin, C. T. Biodegradable polymers as biomaterials. *Prog. Polym. Sci.* **32**, 762–798 (2007).
29. Rudnik, E. Handbook of biopolymers and biodegradable plastics 213-263 (William Andrew Publishing, Boston, 2013).
30. Cutright, D. E., Beasley, J. D. & Perez, B. Histologic comparison of polylactic and polyglycolic acid sutures. *Oral. Surg. Oral. Med. Oral. Pathol.* **32**, 165–173 (1971).
31. Sekitani, T. et al. A large-area wireless power-transmission sheet using printed organic transistors and plastic MEMS switches. *Nat. Mater.* **6**, 413–417 (2007).
32. Omuro, A. & DeAngelis, L. M. Glioblastoma and other malignant gliomas: A clinical review. *J. Am. Med. Assoc.* **310**, 1842–1850 (2013).
33. Nagasawa, D. T. et al. Temozolomide and other potential agents for the treatment of glioblastoma multiforme. *Neurosurg. Clin. North Am.* **23**, 307–322 (2012).
34. Budday, S. et al. Mechanical properties of gray and white matter brain tissue by indentation. *J. Mech. Behav. Biomed. Mater.* **46**, 318–330 (2015).
35. Yuk, H., Zhang, T., Lin, S., Parada, G. A. & Zhao, X. Tough bonding of hydrogels to diverse non-porous surfaces. *Nat. Mater.* **15**, 190–196 (2015).

36. Pramod, P. S., Shah, R. & Jayakannan, M. Dual stimuli polysaccharide nanovesicles for conjugated and physically loaded doxorubicin delivery in breast cancer cells. *Nanoscale* **7**, 6636–6652 (2015).
37. Tangpong, J. et al. Doxorubicin-induced central nervous system toxicity and protection by xanthone derivative of Garcinia mangostana. *Neuroscience* **175**, 292–299 (2011).
38. Bettinger, C. J. & Bao, Z. Organic thin-film transistors fabricated on resorbable biomaterial substrates. *Adv. Mater.* **22**, 651–655 (2010).
39. Son, D. et al. Bioresorbable electronic stent integrated with therapeutic nanoparticles for endovascular diseases. *ACS Nano*. **9**, 5937–5946 (2015).
40. Lee, N. et al. Water-dispersible ferrimagnetic iron oxide nanocubes with extremely high r2 relaxivity for highly sensitive *in vivo* MRI of tumors. *Nano Lett.* **12**, 3127–3131 (2012).
41. Fung, L. K., Shin, M., Tyler, B., Brem, H. & Saltzman, W. M. Chemotherapeutic drugs released from polymers: distribution of 1,3-bis(2-chloroethyl)-l-nitrosourea in the rat brain. *Pharm. Res.* **13**, 671–682 (1996).
42. Pardridge, W. M. Drug transport in brain *via* the cerebrospinal fluid. *Fluids Barriers CNS*. **8**, 7–7 (2011).
43. Bischof, J. C. et al. Dynamics of cell membrane permeability changes at supraphysiological temperatures. *Biophys. J.* **68**, 2608–2614 (1995).
44. Wang, H. et al. Brain temperature and its fundamental properties: a review for clinical neuroscientists. *Front. Neurosci.* **8**, 307 (2014).
45. White, M. G. et al. Cellular mechanisms of neuronal damage from hyperthermia. *Prog. Brain Res.* **162**, 347–371 (2007).
46. Landon, C. D., Park, J.-Y., Needham, D. & Dewhirst, M. W. Nanoscale drug delivery and hyperthermia: the materials design and preclinical and clinical testing of low temperature-sensitive liposomes used in combination with mild Hyperthermia in the treatment of local cancer. *Open Nanomed. J.* **3**, 38–64 (2011).
47. Brown, T. J. et al. Association of the extent of resection with survival in glioblastoma: a systematic review and meta-analysis. *JAMA Oncol.* **2**, 1460–1469 (2016).
48. Inoue, S. et al. Novel animal glioma models that separately exhibit two different invasive and angiogenic phenotypes of human glioblastomas. *World Neurosurg.* **78**, 670–682 (2012).
49. Onishi, M. et al. Annexin A2 regulates angiogenesis and invasion phenotypes of malignant glioma. *Brain Tumor Pathol.* **32**, 184–194 (2015).
50. Otani, Y. et al. Fibroblast growth factor 13 regulates glioma cell invasion and is important for bevacizumab-induced glioma invasion. *Oncogene*. **37**, 777–786 (2018).

Acknowledgements

This work was supported by IBS-R006-A1 and IBS-R006-D1. This work was also supported by Creative-Pioneering Researchers Program through Seoul National University (SNU). N.L., L.W. and S.Q. acknowledge the financial support from the US Office of Naval Research (ONR) under Grant No. N00014-16-1-2044. The Korea Basic Science Institute (Seoul) is acknowledged for the HPLC data.

Author contributions

J.L., H.R.C., G.D.C. and H.S. designed the experiments. J.L., H.R.C., G.D.C., H.S., S.L., C.-K.P., J.W.K., S.Q., L.W., D.K., T.K., J.K., H.L., W.L. and S.H.C. performed experiments and analysis. S.L. and S.H.C. established the animal models. S.K. performed the electromagnetic simulation and analysis. S.-T.L. analyzed the electrophysiology data. T.I. provided the canine glioblastoma cell line (J3T-1). J.L., H.R.C., G.D.C., H.S., N.L., T.H., S.H.C. and D.-H.K wrote the paper.

Competing interests

The authors declare no competing interests.

Additional information

Supplementary information is available for this paper at https://doi.org/10.1038/s41467-019-13198-y.

Correspondence and requests for materials should be addressed to S.H.C. or D.-H.K.

Reprints and permission information is available at http://www.nature.com/reprints

Peer Review Information *Nature Communications* thanks Henry Brem, Martine Roussel and the other, anonymous, reviewer for their contribution to the peer review of this work. Peer reviewer reports are available.

Publisher's note Springer Nature remains neutral with regard to jurisdictional claims in published maps and institutional affiliations.

Supplementary Information

Flexible, Sticky, and Biodegradable Wireless Device for Drug Delivery to Brain Tumors

Jongha Lee *et al.*

Supplementary Methods

1.1. Theoretical analysis of the wireless thermal actuation

Electromagnetic simulations were performed using High Frequency Electromagnetic Field Simulation (HFSS) software to reveal the eddy current distribution following the external wireless mild-thermic actuation. The magnetic field generated from the transmission coil can be calculated as follows. The magnetic field intensity (B_1) generated from the coil is expressed as,

$$B_1 = \frac{\mu_0 I\, a^2}{(a^2 + h^2)^{1.5}} \tag{1}$$

where h is the distance from the center of the coil, a is the radius of the coil, I is the current of the coil, and μ_0 is the permeability of vacuum. If the coil has several turns, the total sum of the magnetic field (B) can be calculated as,

$$B = \sum_{i=1}^{N} \frac{\mu_0 I\, a^2}{(a^2 + h_i^2)^{1.5}} \tag{2}$$

where N is the turn number of the coil. For simplification, the distances from each turn of the coil to the heater, h_i, can be considered to be same as h. Then the equation becomes as follows,

$$B = N \frac{\mu_0 I\, a^2}{(a^2 + h^2)^{1.5}} \tag{3}$$

Using Supplementary Equation 3, the relation between the magnetic field and the temperature increase can be plotted as shown in Supplementary Fig. 13c. We assumed the magnetic field to be constant over the small area of the heater with the diameter of 12 mm at the distance of 3 cm from the coil (Quasi-static assumption). Internal layers between the transmission coil and the heater are modeled as a nonmagnetic material. Then the eddy current is calculated as,

$$J_\phi(\rho) = \frac{\sigma \omega B(\rho) \rho}{2} \tag{4}$$

where J is the eddy current, ρ is the distance from the center of the heater, σ is the electrical conductivity of the Magnesium, ω is the frequency of the coil. Although the eddy current of the BEP with holes cannot be solved analytically, a simple assumption, the round heater model without holes, can be introduced for identifying the relationship between variables. Then, the Joule heating amount is as follows,

$$W = \int \frac{J_\phi^2}{2\sigma} dv = \frac{\pi\sigma t\ \omega^2 B^2 D^4}{256} = \frac{N^2\omega^2\mu_0^2 I^2\ a^4 D^4}{(a^2+h^2)^3}\frac{\pi\sigma t}{256} \quad (5)$$

where W is the amount of the heat generation that is determined by the coil-to-heater distance (h), current of the transmission coil (I), number of the coil turn (N), coil radius (a), RF frequency (ω), heater thickness (t), and heater diameter (D). According to the Supplementary Equation 5, the heat generation is proportional to the square of the coil current and the square of the RF frequency. Since N, a, and ω are fixed by the instrument (magnetic field generator), the key design parameters are the thickness (***t***) and diameter (***D***) of the wireless heater. The other parameters, coil-to-heater distance (h) and current in transmission coil (I), can also be optimized during the experiment.

For the analysis of the round heater with the hole array, the HFSS simulation is used. The heaters of three different diameters show similar amount of heat generation under the three different frequencies, which shows the potential for further minimization of the wireless heater (Supplementary Fig. 13e and f).

1.2. Modeling of the three-dimensional (3D) thermal profile and DOX diffusion.

Finite element modeling of 3D thermal profiles at various heater temperatures. Finite element simulations were performed using COMSOL5.2 to reveal the temperature distribution following wireless mild-thermic actuation of the heater to accelerate drug delivery.

The brain tissue was simplified to be only represented by white matter, which consists of 75% (*w/w*) water, 9% (*w/w*) protein, and 16% (*w/w*) fat. After calculating the effective thermophysical properties of this tissue, we simply modeled it as a single layer with infinite thickness and homogeneous thermophysical properties. Similarly, the drug reservoir (77% *w/w* starch and 23% *w/w* glycerol) was modeled as a layer with effective thermophysical properties. Both the heater and the drug reservoir are encapsulated by cerebrospinal fluid, which was

modeled as water for the sake of simplicity. Details of the thickness, heat capacity, heat conductivity, and mass density of each BEP layer are described in Supplementary Table 3. The temperature of the brain tissue at infinity was fixed at body temperature (37 °C), while the Mg heater temperature was set at 42 °C. At equilibrium, the temperature distribution within the brain tissue at heater temperature are shown in Fig. 3k as 2D plots. Along the depth direction in the brain, the temperature beneath the center of the BEP was plotted in Fig. 3l, and the shaded part represents the temperature range within which human tissues will not incur heat damage. Thus, Fig. 3l can be used to control the BEP temperature in order to avoid tissue damage.

Modeling of DOX diffusion into the brain and induction heating. The diffusion of DOX into the brain was modeled as an isotropic diffusion process. Due to the significant temperature dependence of cell membrane permeability, we had to account for the temperature dependence of the diffusion coefficient. For the sake of simplicity, we adopted the following linearized diffusivity-permeation relation:

$$D(T) = aP(T) + D_0 \tag{6}$$

where D is the diffusivity of DOX in brain, T is the temperature, P is the permeation of DOX in brain (which was approximated from previously published experimental data,[1] and a and D_0 are constants to be determined. To express the temperature dependence of P explicitly, we fitted the reported experimental data[1] using the modified Lorentzian asymmetric peak fitting method; this is plotted as the red solid curve in Supplementary Fig. 18a. The DOX profile was experimentally measured with the heater on or off after 30 min, 5 h, and 15 h. By fitting the measured DOX profiles, we obtained the brain diffusivity of DOX when T = 37 °C (T_0; body temperature; reference temperature) and when T = 42 °C (Supplementary Fig. 18b and 17c).

$$D(T = 37\ ^\circ\mathrm{C}) = 3\times10^{-13}\ \mathrm{m^2\ s^{-1}}\ D_0 \tag{7}$$

$$D(T = 42\ ^\circ\mathrm{C}) = 9\times10^{-12}\ \mathrm{m^2\ s^{-1}}\ D_0 \tag{8}$$

From this, we calculated that $a = 5.86\times10^{-8}$ and $D_0 = 1.13\times10^{-13}$ m^2 s^{-1} in the $D(T) \sim P(T)$ relation. We assumed that the drug reservoir had a constant DOX concentration (c_0) over time,

and that the ambient/brain interface had no mass flux. Using this time-dependent diffusivity value, the brain DOX profile could be calculated for a particular brain temperature field.

COMSOL was used to calculate the brain temperature field achieved using the induction-heating module. To reduce the computational complexity of 3D induction heating, we simplified the model by reducing the detailed 3D structure of the Mg heater to a 2D structure (Supplementary Fig. 18d) by leveraging the axisymmetry of this problem. The entire BEP/brain system rested in an ambient environment at a room temperature of 20 °C. A 5-turn copper coil was placed above the BEP with an electric current of 360 A (frequency; 220 kHz, Easyheat, Ambrell, USA). The resistivity of the copper coil (ρ_c), was linearized as a function of T:

$$\rho_c = \rho_0[1 + \alpha_T(T - T_0)] \tag{9}$$

where ρ_0 was the reference resistivity of copper (1.76×10^{-8} Ωm), α_T was the temperature coefficient (0.0039 K^{-1}), and T_0 = 20 °C (the reference temperature). Cooling water ran through the induction coil and this was expressed as:

$$Q_0 = \frac{M_t C_p (T_{in} - T)}{2\pi r A} \tag{10}$$

where M_t is the inlet flow rate (15 kg min^{-1}), T_{in} is the inlet temperature (293 K), C_p is the heat capacity of water (4187 J kg^{-1} K^{-1}, r is the radial position of the coil, and A is the cross-sectional area of the coil. The coil had inner and outer radii of 20 mm and 25 mm, respectively, and its cross-section was a circular ring with an inner radius of 1.5 mm and a thickness of 1 mm.

When modeling the inductive heating, the whole domain was considered to be governed by Ampere's law and heat transfer; this included the air, coil, BEP, and brain tissue. At the extremities of the air and brain domains, magnetic insulation boundary conditions were used to calculate the magnetic field. The temperatures in the depth direction were set at room temperature (20 °C) for the air and body temperature (37 °C) for the brain. Lateral heat flux was calculated using

$$q = h\Delta T \tag{11}$$

where the heat transfer coefficient (h) was 5 W m^{-2} K^{-1} for the air domain and 10 W m^{-2} K^{-1} for

the brain domain.

For this inductive heating-diffusion problem, we assumed that the inductive heating achieved equilibrium much faster than the diffusion process. Thus, the coupled magnetic-temperature field was first solved using the frequency-stationary method; the resultant temperature field was then used in the diffusion model, which was solved using a time-dependent method in COMSOL. A contour plot of the temperature distribution in the whole system is shown in Fig. 3k, where the distance between the bottom of the coil and the surface of the brain was set to be 2 cm. The normalized DOX profile in the brain for the same coil-brain distance is provided in Supplementary Fig. 18e. The distance between the coil and the brain is a tunable parameter that could be used to control the heating power.

Finite element modeling of 3D thermal profiles at various skull thickness. Finite element simulations were performed using COMSOL 5.2 to reveal the heater temperature in various conditions of skull thickness.

The brain tissue was simplified to be only represented by white matter, and surrounding environments are same as "***Finite element modeling of 3D thermal profiles at various heater temperatures***"**.** Details of the thickness, heat capacity, heat conductivity, and mass density of each BEP layer are described in Supplementary Table 3. For the sake of simplicity, we use the same material properties for human, canine, and mouse skulls as listed in the Supplementary Table 4. Relative permittivity, density and electric conductivity is approximated by porcine and ovine skull measurements[2, 3]. Thermal conductivity is approximated by measurements on the shoulder blade of a pig, and sheep skull[4]. As shown in Supplementary Fig. 19, the elevated temperature of the heater is independent regardless of the skull thickness.

1.3. Wireless temperature sensor.

The wireless temperature sensor was designed as an LC oscillator made of Mg and PLGA (lactic acid:glycolic acid; 65:35) was used as the dielectric material because its glass transition temperature is ~39 °C, which is close to the body temperature. As the temperature increases above the body temperature, the glass transition changes the morphology of PLGA, resulting in a change in the dielectric permeability. This also changes the resonance frequency of the LC oscillator. Thus, a temperature change was detected by observing the change of the sensor resonance frequency. A conventional inductor coil was used as a reader coil to detect the resonance frequency change of the sensor wirelessly. Inductance coupling between the sensor

and the reader coil occurs when they are close to each other and in parallel. As the resonance frequency of the sensor responds to the temperature increase, the resonance peak of the inductively coupled reader coil is also altered. Therefore, the BEP temperature change was wirelessly monitored by observing the resonance peak of the reader coil with a Network Analyzer (Agilent B1500A, Agilent Technologies, USA).

1.4. Mouse subcutaneous GBM model.

This study was approved by our Institutional Animal Care and Use Committee (IACUC; No. 14-0156-C1A3) and was performed in accordance with our IACUC guidelines and with the National Institute of Health Guide for the Care and Use of Laboratory Animals. The researchers who carried out surgery, managed the animal, and measured the tumor volume were blinded each other.

Implantation of human glioblastoma cells into mice. Thirty-three 6-week-old female BALB/c nude mice weighing approximately 20–25 g were used in this study. Prior to tumor implantation, the animals were sedated with an intramuscular injection of 5 mg of a 3:1 combination of tiletamine hydrochloride and zolazepam (Zoletil; Virbac, Carros, France) and xylazine hydrochloride (Rompun 2%; Bayer Korea, Korea) per kg body weight. Then, U87-MG cells were subcutaneously transplanted (2×10^5 cells/100 μL medium/mouse) into the thigh of the nude mice.

Subcutaneous implantation of BEP. Fourteen days after implantation, human U87-MG tumors implanted in BALB/c nude mice had grown to a radius of ~4 mm. The tissues were exposed and resected, leaving ~ 30 mm^2 of tumor. A BEP (12 mm in diameter) containing 0.69 mg DOX was then implanted onto the residual tumor (Supplementary Fig. 21). During the treatment period, the tumor volume was tracked by MR imaging every week. The tumor area in each MR image slice was measured and multiplied by the layer thickness (1 mm). Then the summation of the volume from each slice was regarded as a total tumor volume. Four different treatment groups were used to investigate the therapeutic effects of BEP: a control IV group received an intravascular injection of the equivalent amount of DOX, immediately after resection surgery; the Heating group received an implantation of BEP containing no DOX, with wireless mild-thermic actuation; the OST group received an implantation of BEP containing DOX, without mild-thermic actuation; and the OST+Heating group received an

implantation of BEP containing DOX, with mild-thermic actuation. The groups receiving wireless heating were treated for 30 min daily for 14 days.

MR image acquisition. The tail vein was catheterized after anesthesia with 1.5-2% isoflurane/oxygen (*v/v*), and the animals were placed in a 9.4 T MR image scanner (Agilent Technologies, USA). Throughout each imaging session, the animals were wrapped in a warm water blanket and their oxygen saturation and heart rates were monitored. A millipede 1-ch coil was used for both radio frequency transmission and signal reception (Agilent Technologies, USA) and a fast spin echo sequence was used to produce a T2-weighted image. The measurement parameters were as follows: repetition time = 3000 ms; effective echo time = 30.82 ms; field-of-view = 20×35 mm; echo train length = 4; matrix = 256×256; slice thickness = 1.0 mm.

1.5. Mouse brain GBM model.

This study was approved by the Institutional Animal Care and Use Committee (IACUC; No. 14-0156-C1A3) and was performed in accordance with the IACUC guidelines and with the National Institute of Health Guide for the Care and Use of Laboratory Animals.

In this study, human glioblastoma cell line U87-MG which was obtained directly from ATCC (HTB-14) was used for GBM model. Before implantation, the cell line was re-authenticated using microsatellite profiling and routinely tested to exclude infection with mycoplasma.

For mouse GBM model, we examined 15 male BALB/c nude mice (mean weight, 20 ± 25 g). The mice were anesthetized with a mixture of zolazepam and xylazine and were placed in a stereotaxic device. Total 3×10^6 cells were injected per mouse using a Hamilton syringe fitted with a 28-gauge needle, which was positioned by the stereotaxic device. The following coordinates with the stereotaxic guidance were used: AP -1.3 mm, ML +2.0 mm, and DV -1.0 mm. A week after cranial implantation, intracranial implantation of device was performed.

Intracranial implantation of devices. A 2 mm diameter and 1 mm height gold heater was attached to the OST film of 3 mm diameter. The OST film contained 0.13 mg DOX. The control wafer containing 0.88 mg carmustine was also implanted. After fixing the mouse head position, we cut the skin of the head and drilled the mouse skull in a round shape for implantation of the patch. Devices were implanted on the tumor tissue, and then their positions were fixed using N-butyl cyanoacrylate (Supplementary Fig. 23c). During the treatment period, the tumor

volume was tracked by MR imaging every week. Three different treatment groups were used to investigate the therapeutic effect in the brain microenvironment: The sham operating group received a physical surgery protocol and anesthesia like different groups but without implantation; the control wafer group received implantation of the control wafer containing carmustine without mild-thermic actuation; and the OST+Heating group received implantation of the gold heater and OST film containing DOX with mild-thermic actuation (30 min daily for 14 days).

MR image acquisition. After anesthesia with 1.5/2% isoflurane/oxygen (v/v), the animals were placed in a 9.4 T MR image scanner (Agilent Technologies, USA). Throughout each imaging session, the animals were wrapped in a warm water blanket and their oxygen saturation and heart rates were monitored. A Rapid 1H surface Coil (RAPID Biomedical GmbH, Rimpar, Germany) was used for both radio frequency transmission and signal reception (Agilent Technologies, USA) and a fast spin echo sequence was used to produce a coronal T2-weighted image. The measurement parameters were as follows: repetition time = 3000 ms; effective echo time = 31.18 ms; field-of-view = 25×25 mm; echo train length = 4; matrix = 256×256; slice thickness = 1.0 mm.

Mild-thermic actuation and therapeutic efficacy. The gold heater on the OST film provides sufficient heating (Supplementary Fig. 23f) for mild-thermic actuation (ΔT = 5 °C). Compared to the control, recurrence of brain tumor was suppressed (p = 0.0317; Supplementary Fig. 23g-j) in the 'OST+heating' group. The survival time was also prolonged in the 'OST+Heating' group compared to the control (p = 0.0011; Supplementary Fig. 23k).

1.6. Canine GBM model.

This study was approved by our Institutional Animal Care and Use Committee (IACUC; No. 14-0156-C2A3) and was performed in accordance with our IACUC guidelines and with the National Institute of Health Guide for the Care and Use of Laboratory Animals.

Preparation of canine brain tumor fragments for implantation. J3T-1 cells were prepared in 100 mL serum-free RPMI medium and then subcutaneously transplanted (2×10^5 cells/100 μL medium/mouse) into the shoulders of 6-week-old female BALB/c nude mice (Koatech, Korea). The mice were sacrificed 14 days after the injection, and tumors were extracted to

make fragments of 20 mm in diameter, which were washed with phosphate-buffered saline (PBS) and suspended in 50% basement membrane matrix (Matrigel, BD Bioscience, USA) in an icebox. For each dog, 10 brain tumor fragments of 3–5 mm in diameter were prepared for implantation.

Canine brain tumor implantation. 2 Adult male mongrel dogs per group (International Laboratory Animal Center, Korea) weighing approximately 10–12 kg were used in this study. Each dog was treated with immunosuppressive agents before tumor implantation and for the duration of the study. For immunosuppression, the dogs were treated for 7 days with an oil-based cyclosporine formulation (Sandimmune; Novartis Pharm., Switzerland) (400 mg orally, twice daily). In addition, 50 mg of azathioprine (Azaprine Tab., Korea United Pharm. Inc., Korea) and 10 mg of prednisolone (Solondo Tab., YuhanMedica, Korea) were mixed with normal saline and then administered orally twice daily. This regimen was previously used in an intraparenchymal and cavernous sinus tumor model in canines[5, 6].

After 7 days of immunosuppressive agent administration, tumor implantation was performed in the dogs (Supplementary Fig. 24). The animals were first sedated with an intravenous injection of 5 mg of a 1:1 combination of tiletamine hydrochloride and zolazepam (Zoletil; Virbac, Carros, France) and xylazine hydrochloride (Rompun 2%; Bayer Korea, Korea) per kg of body weight. The dogs were then intubated and placed on a ventilator. Anesthesia was maintained with isoflurane at a concentration of 0.5–3%, depending on the vital signs observed during surgery.

The scalp was shaved, scrubbed, and draped in an aseptic manner prior to making a scalp incision over the right frontoparietal region. The muscle was split with cautery and retracted. The underlying cranium was exposed, and a craniotomy was performed to create a burr hole (0.3–0.5 cm in diameter) using a handpiece drill (STRONG 204; Saeshin Precision Co., Ltd., Korea). After confirming the dural layer from the base of hole, the prepared tumor fragments were implanted in the right frontal lobe of each dog using an 18-gauge spinal needle. Bleeding from the procedure was controlled using bone wax (ETHW31G, Ethicon, USA) or *N*-butyl cyanoacrylate (Histoacryl, Braun, Germany). The overlaying muscle and skin were then closed using a 3-0 Vicryl suture and a 4-0 nylon suture.

All dogs were given intramuscular injections of cephazolin (Cefazolin; Chong Kun Dang Pharm. Co., Korea) to prevent infection, and surgical sites were swabbed with povidone-iodine was applied onto the surgical site for 7 days. Leukocyte and C-reactive protein counts were

measured routinely to detect potential infections or signs of sepsis.

Intracranial bioresorbable electronic patch (BEP) implantation. Seven to fourteen days after tumor implantation, canine brain tumors had grown to 1–2 cm in the longest dimension. Prior to surgery, anesthesia was induced as described above, and then a scalp incision was widely made over the right frontoparietal region along the previous incision site, under aseptic conditions. When the underlying cranium was exposed, a craniectomy was performed to establish the surgical view at the location of the tumor around the previous craniotomy site using a handpiece drill. The remaining bone was removed using a surgical elevator, and the dura was carefully dissected using micro scissors to expose the brain parenchyma. After careful removal of the brain parenchyma using bipolar forceps, the location of the tumor was matched with the magnetic resonance (MR) image, and finally the tumor was exposed. Tumor tissues were resected almost entirely, leaving microscopic residual tumor tissues (Supplementary Fig. 25). Then, the BEP (12 mm in diameter, containing 1 mg DOX) or control wafer (containing 2.38 mg carmustine) was positioned to cover the residual tumor sufficiently, and fixed with surgical glue (*N*-butyl cyanoacrylate; *Histoacryl*, Braun, Germany) (Supplementary Fig. 24). The muscles and skin were then sutured as described above.

MR image acquisition. MR imaging was performed using a 3.0 T MR imaging system (Magnetom Trio; Siemens Medical Solutions, Germany) with a human head coil. Prior to MR imaging, anesthesia was induced as described above. All MR imaging examinations were performed with the dogs in the supine position and included the entire brain.

The brain imaging sequences included axial turbo-spin echo T2-weighted images (T2WI), axial gradient-echo T1-weighted images (T1WI), and axial contrast-enhanced (CE) T1WI. After routine localization images were obtained, T2WI (repetition time/echo time, 5160 ms/91 ms; flip angle 131°, section thickness, 5 mm; matrix, 640×290) and T1WI (repetition time/echo time, 990 ms/9.8 ms; flip angle 70°, section thickness, 1.5 mm; matrix, 384×212) were acquired. Subsequently, CE T1WI was acquired after an intravenous injection of 0.2 mL/kg godoteric acid (Dotarem; Guerbet, France) via the cephalic vein.

2.1. Materials.

All of the materials were used as purchased, unless stated otherwise. Starch from corn (unmodified waxy corn starch of essentially pure amylopectin), sodium periodate ($NaIO_4$),

PLA (M_w ~ 260,000), PLGA (lactic acid:glycolic acid; 65:35; M_w 40,000-75,000), PBS, polyimide precursor solution (poly(pyromellitic dianhydride-co-4,4′-oxydianiline), amic acid solution (electronic grade), and 1-methyl-2-pyrrolidinone (> 99%) were purchased from Sigma Aldrich (USA). Glycerol was purchased from Samchun Chemical (Korea), DOX·HCl was purchased from Ildong Pharm (Korea), and polydimethylsiloxane base with curing agent (Sylgard 184) was purchased from Dow Corning (USA).

For device fabrication, the thermal evaporating source of Mg (> 99.5%) was purchased from Taewon Scientific Co. (Korea), the sputter target of ZnO (99.99%) was purchased from Thifine (Korea), the Si wafer was purchased from 4Science (Korea), poly(methylmethacrylate) (PMMA A11) was purchased from MicroChem (USA), and positive photoresist S1805, AZ5214, and AZ4620 were purchased from AZ Electronics Materials (USA).

2.2. Synthesis of OST.

$NaIO_4$ was used as the reducing agent for the synthesis of OST. First, 2.14 g $NaIO_4$ was dissolved in 250 mL water before adding various amounts of starch. Next, hydrochloric acid was used to adjust the pH to 3-4. The solution was strongly stirred overnight at 40 °C, and the resultant OST was filtered and washed 3 times with 0 °C deionized water. The final OST product was dried for 24 h at 40 °C under a vacuum.

2.3. Fabrication of starch and OST films containing DOX.

To produce a normal starch patch containing DOX, 1.5 g starch powder, 50 mg DOX, and 0.45 g glycerol were dissolved in 40 g water at 80 °C. The mixture was stirred for 30 min until a clear solution was obtained. The solution was then poured into a petri dish (90-mm diameter) and dried at 65 °C with 80% humidity for 48 h.

To produce an OST film containing DOX, 1.5 g OST powder and 50 mg DOX were dissolved in deionized water and strongly stirred for 24 h at 80 °C to form the imine linkage between OST and DOX. Glycerol (0.45 g) was then added to the mixture and after 1 h, the solution was poured into a petri dish and dried, as described above.

2.4. Flexibility of OST films containing various glycerol concentrations.

Dried OST films fabricated using a range of glycerol concentrations were cut into rectangles of 5×50 mm^2. Each end of the patch was fixed to a digital force gauge (Series 4, Mark-10, USA) and stretched at a speed of 20 mm/min until it fractured. The elastic modulus was

calculated from the slope of stress-strain curve and the maximum length was achieved at the rupture point.

2.5. Adhesion force between tissue and OST films containing various concentrations of reducing agent.

Dried OST films fabricated using different levels of aldehyde were cut into rectangles of 10×20 mm^2. One side of each film was attached to bovine muscle as a representative biological tissue; this was used because the adhesion force between the patch and brain tissue was larger than the internal coherence of the brain tissue. The other side of the film was fixed to a digital force gauge (Series 4, Mark-10, USA) and a shear force was applied at a speed of 10 mm/min until the film was detached from the muscle. The shear stress at failure was calculated.

2.6. DOX release profiles from starch and OST *in vitro*.

The DOX release profiles were determined by measuring the absorbance of the solution at 480 nm using SpectraMax M3 (Molecular Devices, USA). Each patch was the same size (20×20 mm^2) and contained 3.387 mg DOX. Each patch was placed in 50 mL PBS and the DOX concentration was measured over time (n = 4). The 500 μL of PBS was extracted from the 50 mL solution for the measurement every day, and the entire PBS was replaced every 2 days to mimic *in vivo* cerebrospinal circulation[7]. The concentration was divided by the decreased volume in the concentration calculation. The released DOX was determined using a standard curve of DOX concentration versus absorbance, and cumulative release was calculated by integrating these measurements.

2.7. Measurement of DOX diffusion using fluorescence microscopy.

The implanted BEP was retrieved and the tumor tissue was extracted. Tissue blocks of the entire tumor were cut, embedded in optimal cutting temperature compound, and stored at -80 °C. Ten 10 μm serial frozen sections were obtained and examined using fluorescence microscope (DM5500 B, Leica, Germany) and camera (DFC365 FX, Leica, Germany) with filter sets for DOX (excitation/emission: 488/520 nm). All DOX diffusion profiles are measured by this method.

2.8. Wireless RF heating performance of the heater.

The performance of heaters of different sizes was evaluated using an infrared camera (i5, FLIR, USA). The patches were heated by 360 A coils with different distances. When the elevated temperature reached the maximum point and converged, the temperature was measured five times/s by the infrared camera (i5, FLIR, USA).

2.9. DOX diffusion into tumor cells.

In vivo DOX diffusion into tumor cells was monitored by fluorescence imaging. A BEP containing 0.69 mg of DOX was implanted subcutaneously in mice. After each implantation period, the BEP was detached from the tissue, which was then removed for DOX assessment. A 30-min pulse of mild-thermic actuation ($\Delta T = 5$ °C) was used in the relevant experimental groups. The tissue diffusion profiles of DOX were analyzed using LAS AF Lite (LEICA, USA) with a quadrangle block, starting from the BEP-tissue interface and moving into the tissue. The average fluorescence intensities at each distance were transformed into DOX concentrations using calibration. To obtain this calibration, excised fresh tumors ($3\times3\times2$ mm^3) were incubated with 34 μM DOX in PBS for 72 h. The tumors were then removed from the DOX solution and cryosectioned. The remaining DOX concentration was measured using SpectraMax M3 (Molecular Devices, USA), as previously described. The amount of DOX taken up by the tumors was then calculated by subtraction, and equated with the fluorescent intensity of the tumor tissue. The measured concentration-intensity relationship was also used to calibrate the diffusion profile *ex vivo*.

2.10. Neurological tests

In vivo electroencephalography surgery were performed as previously described[8, 9]. This is for detecting whether a severe degree of seizure may occur due to the implanted BEP. For electroencephalographic monitoring, the mice were subjected to electroencephalographic surgery 3 days before the implantation of the BEP. For surgery, the animals were anesthetized by intraperitoneal injection of 1% ketamine (30 mg/kg) and xylazine hydrochloride (4 mg/kg). The surgery was performed using a stereotaxic apparatus (Kopf Instruments, Tujunga, CA, USA). Electroencephalograms were obtained with tungsten electrodes (0.005 inch, 2 MΩ), which were positioned onto the right hemisphere at AP −1.8 mm, L 2.1 mm, and DV 0.8–1.0 mm (cortex) from the bregma with grounding over the cerebellum. The electrical activities were recorded after amplification (×1200), bandpass-filtering from 0.1 to 70 Hz, and digitization at a 400-Hz sampling rate (AS 40) with a digital electroencephalography system

(Comet XL; Astro-Med, Inc., Warwick, RI, USA). Electrophysiological data were analyzed offline using PSG Twin 4.2 (Astro-Med, Inc.). Electroencephalographic signals in the mice were continuously recorded for 2 weeks. The epileptologist interpreted the intracranial electroencephalogram (iEEG) based on the occurrence of rhythmic burst discharges.

Rotarod performance of mice was assessed as previously described[10] for verifying the indirect influence of the BEP implanted adjacent to the motor cortex, such as potential physical and/or chemical damages caused by implantation surgery, intracranial pressure change, and anti-tumor drug release. The accelerating Rota-Rod (San Diego Instruments, San Diego, CA, USA) set to linearly increase the speed from 4 to 40 rpm over 3 min. At baseline (pre), mice were trained on three consecutive days for three trials per day with a rest period of approximately 30 min between trials. The trial was terminated if the animal fell off the rungs or gripped the device and spun around for two consecutive revolutions. At each test day, mice were tested for three trials, and the mean latencies to fall were used for statistical analyses.

Supplementary Figures

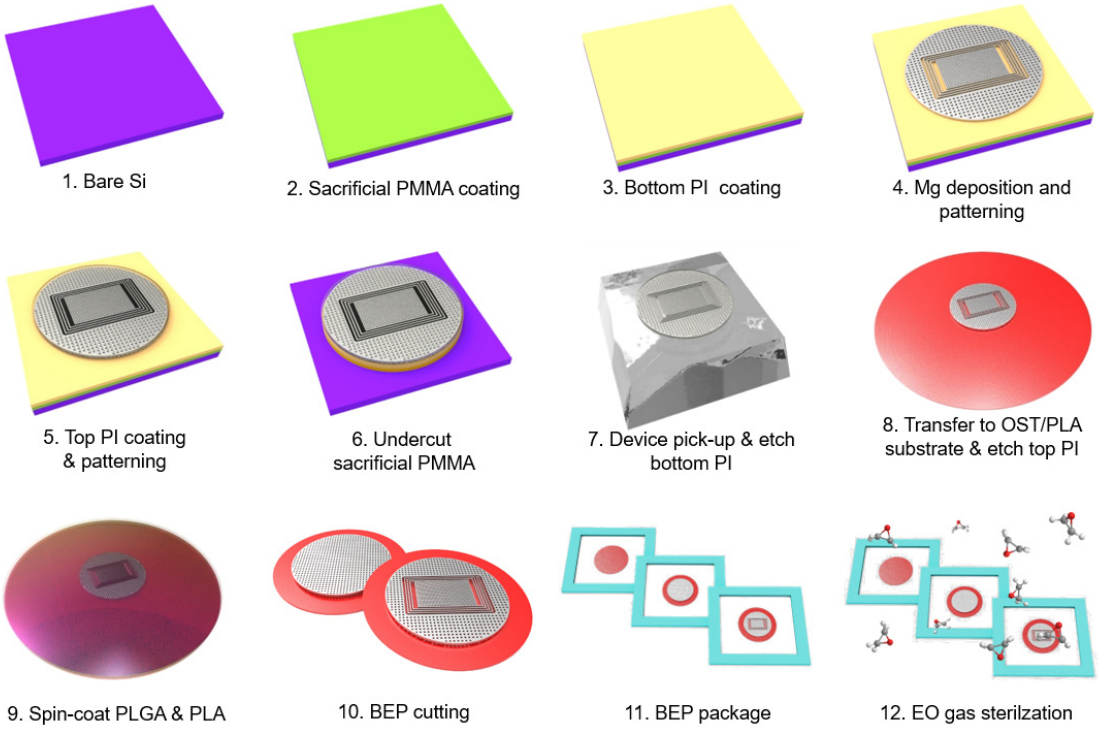

Supplementary Figure 1
Schematic illustration of the BEP fabrication process.

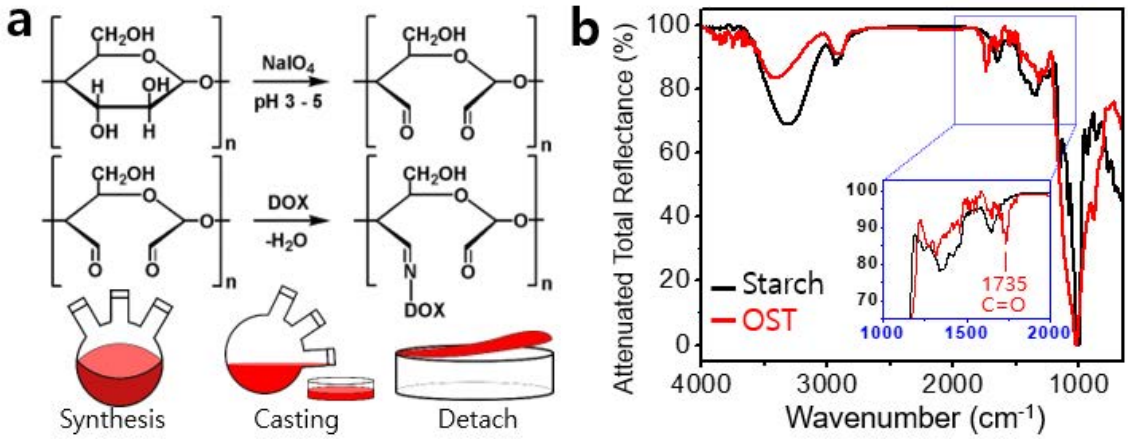

Supplementary Figure 2
(**a**) Synthesis and fabrication of the OST film. (**b**) Infrared spectroscopy analysis of unmodified starch and OST.

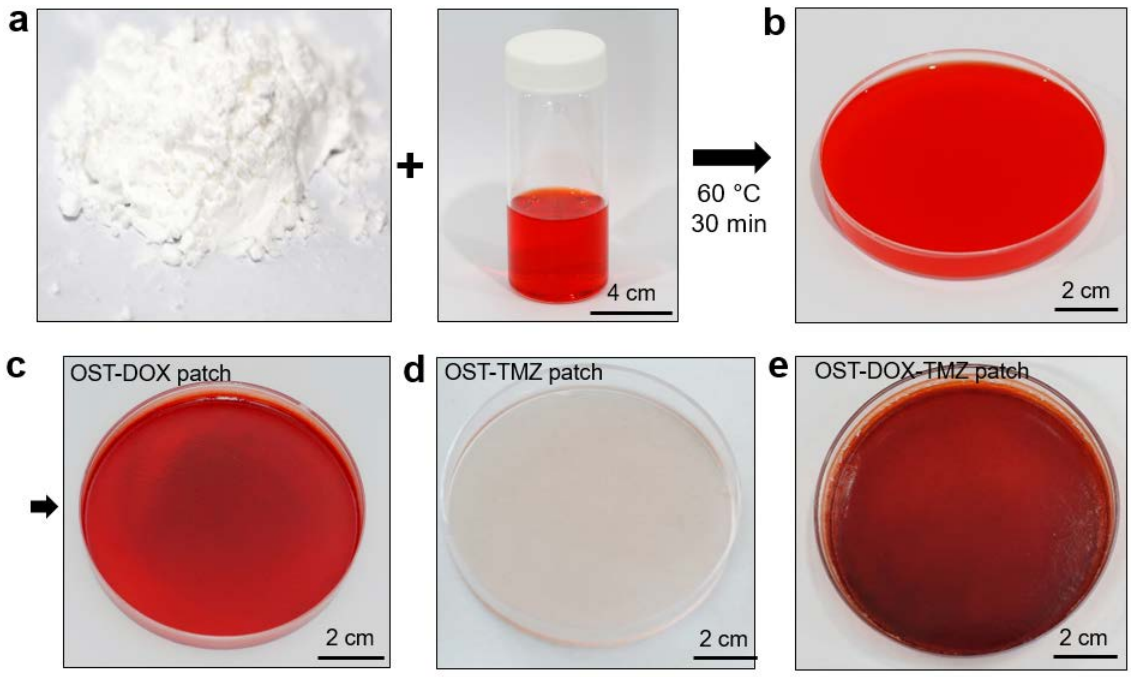

Supplementary Figure 3
Fabrication of the OST film. (**a**) Image of the waxy corn starch powder (left) and DOX solution (right). (**b**) Mixed solution molded in the 90 mm petri dish after heating at 60 °C for 30 min. (**c**) OST-DOX patch dried in the petri dish for 48 hours. (**d**) OST patch containing 20 mg temozolomide (TMZ). (**e**) OST patch containing both 20 mg of DOX and 20 mg of TMZ.

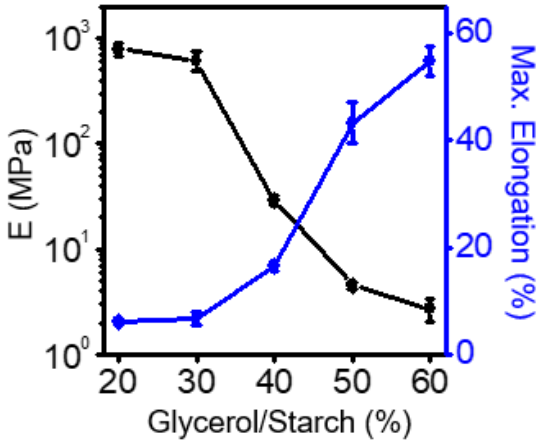

Supplementary Figure 4
Elastic modulus and maximum elongation of the starch film as a function of the glycerol concentration.

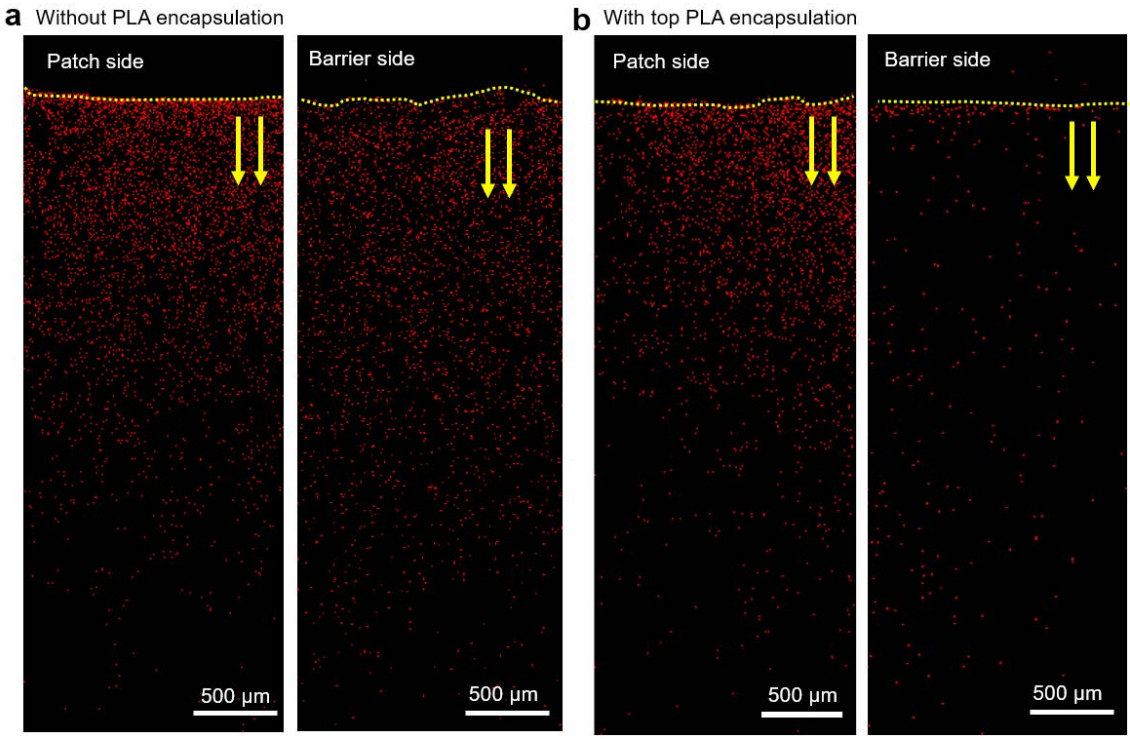

Supplementary Figure 5
Fluorescent images of DOX in the hydrogel that exhibit the amount of drug diffusion from the patch side (left) and the barrier side (right) of the BEP to the hydrogel (agar, 2 wt% in water) at 37 °C. (**a**) BEP without the top PLA encapsulation and (**b**) with the top PLA encapsulation.

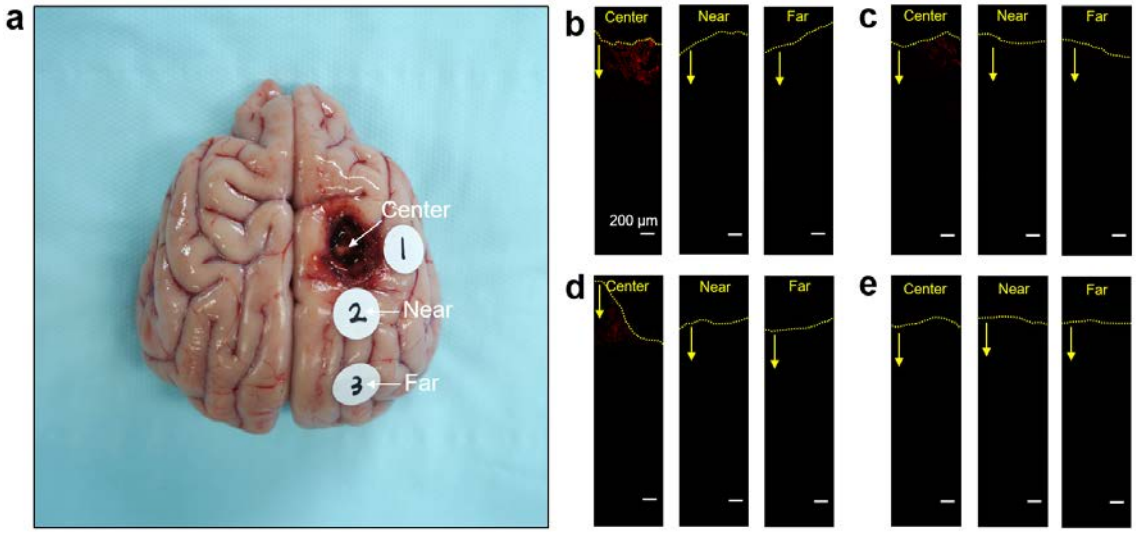

Supplementary Figure 6
Imaging of DOX at three different sites (1: center of the implantation site (the parietal lobe), 2: near the implantation site (the parietal lobe), 3: far from the implantation site (the occipital lobe)) in the canine brain at various time points. (**a**) Gross image of the canine brain at day 1 after the BEP implantation. Fluorescence imaging of DOX at three different sites in the canine brain at (**b**) 1 day, (**c**) 2 weeks, (**d**) 4 weeks, (**e**) 6 weeks after the BEP implantation.

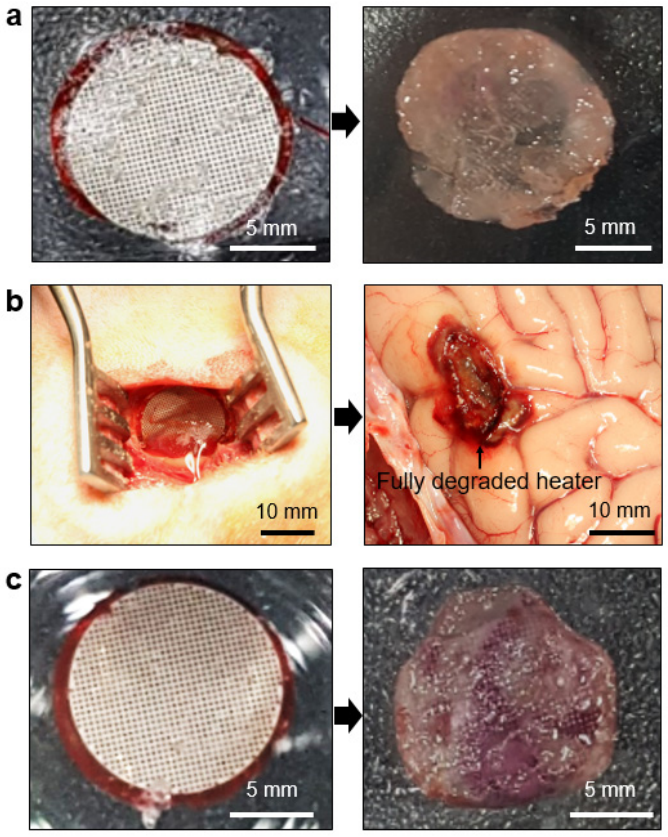

Supplementary Figure 7
The biodegradation of the wireless heater at different time points (left: day 0, right: day 14). Optical images of the biodegradable heater in (**a**) 37 °C PBS, (**b**) canine brain, and (**c**) 42 °C PBS.

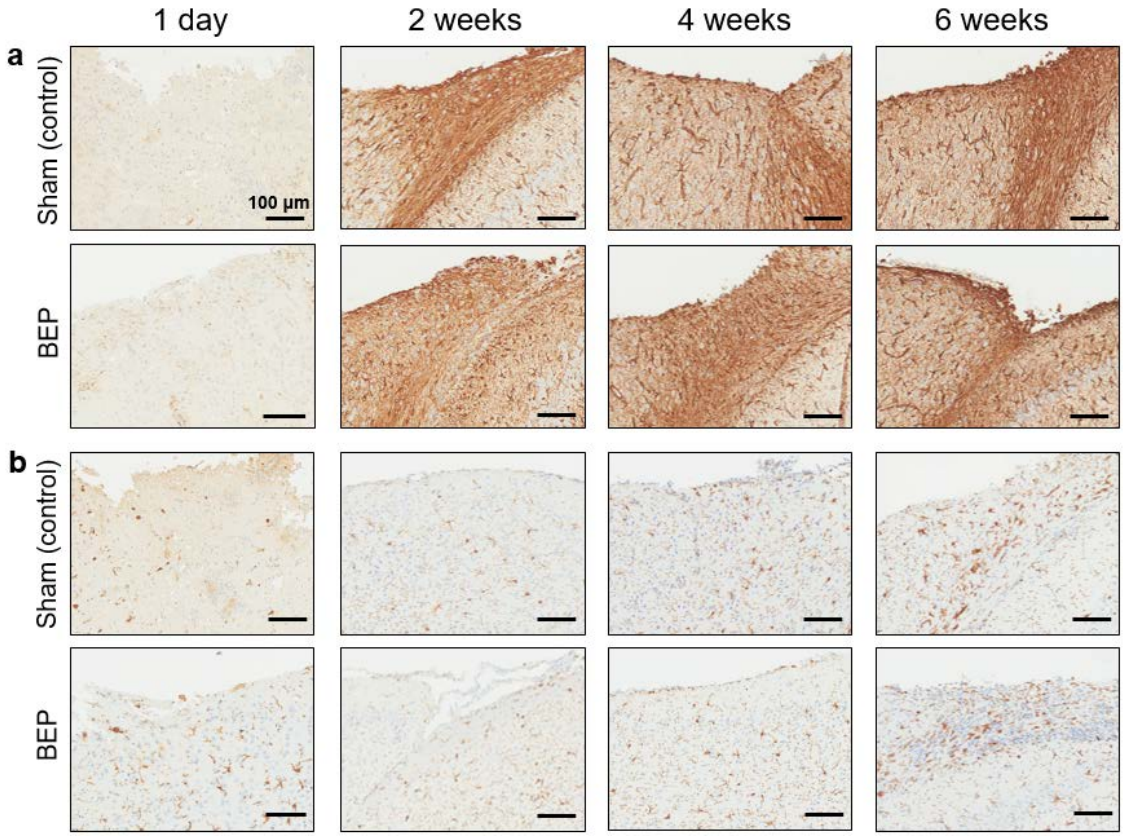

Supplementary Figure 8
(**a**) Confocal fluorescence microscopy images of the GFAP expression in the tissue slices from the implantation site in BALB/c nude mice groups (top for sham and bottom for BEP group) at different time points (1 day, 2 weeks, 4 weeks, and 6 weeks). (**b**) Confocal fluorescence microscopy images of the Iba-1 expression in the tissue slices from the implantation site in BALB/c nude mice groups. Other conditions are same with (**a**).

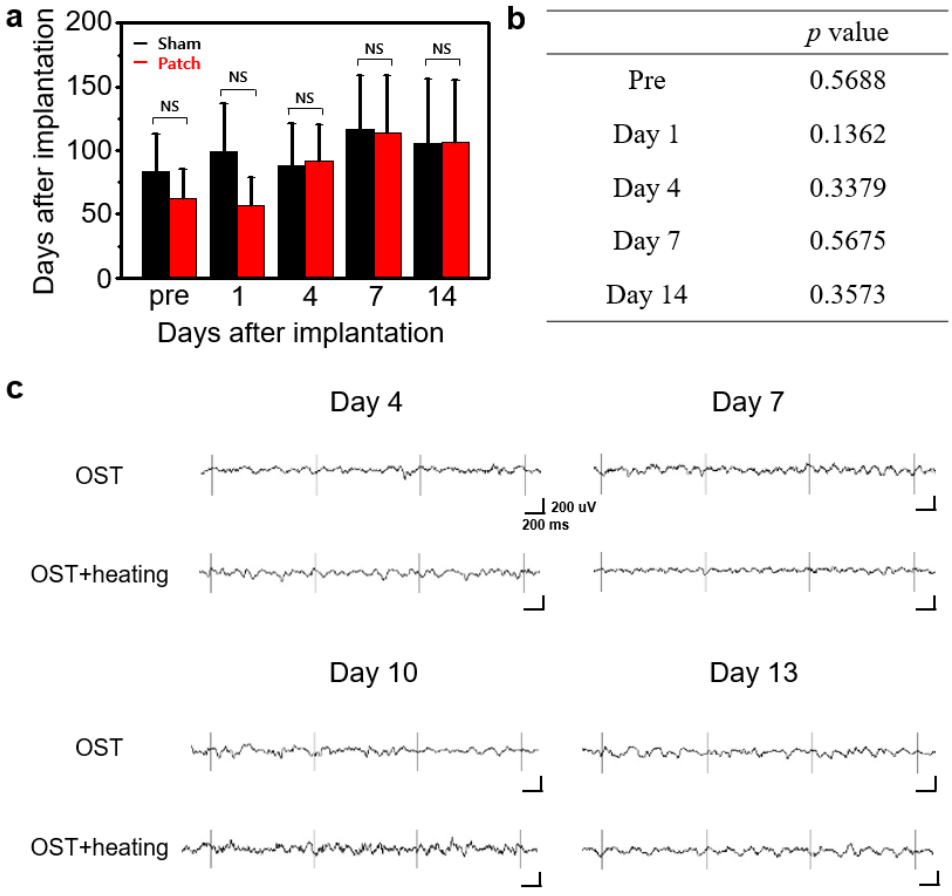

	p value
Pre	0.5688
Day 1	0.1362
Day 4	0.3379
Day 7	0.5675
Day 14	0.3573

Supplementary Figure 9
Neurological test result to examine biocompatibility of the BEP. (**a**) Rotarod retention time of the sham operating group (black line) and the BEP implantation group (red line) at various time points after the surgery. Error bars represent the standard error of the mean value. n = 5, 6 for the sham and BEP implantation group. (NS; $p > 0.05$ by paired t-test) (**b**) *p*-values of the rotarod retention time in the sham and BEP implantation group at different time points, which are calculated by the paired t-test. (**c**) Intracranial electroencephalograms (iEEGs) of the sham operating group and the BEP implantation group at different time points.

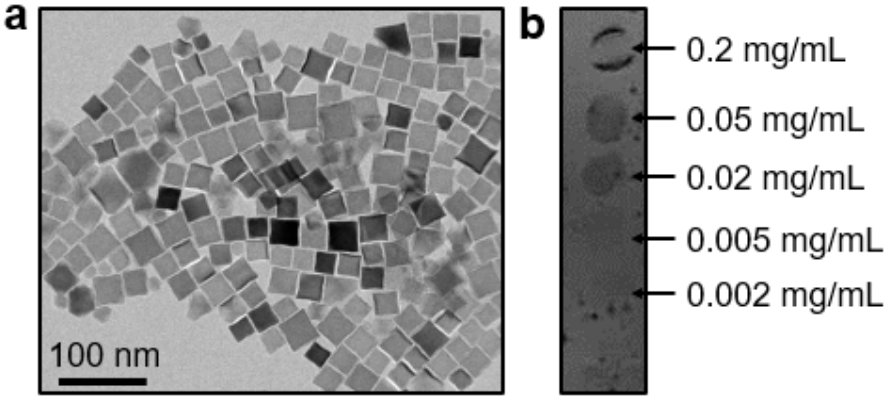

Supplementary Figure 10
Ferrimagnetic iron oxide nanocubes (FION) as the magnetic resonance (MR) contrast agent for intracranial bioresorption monitoring.
(**a**) Transmission electron microscope image of FION. (**b**) FION concentrations versus contrast values.

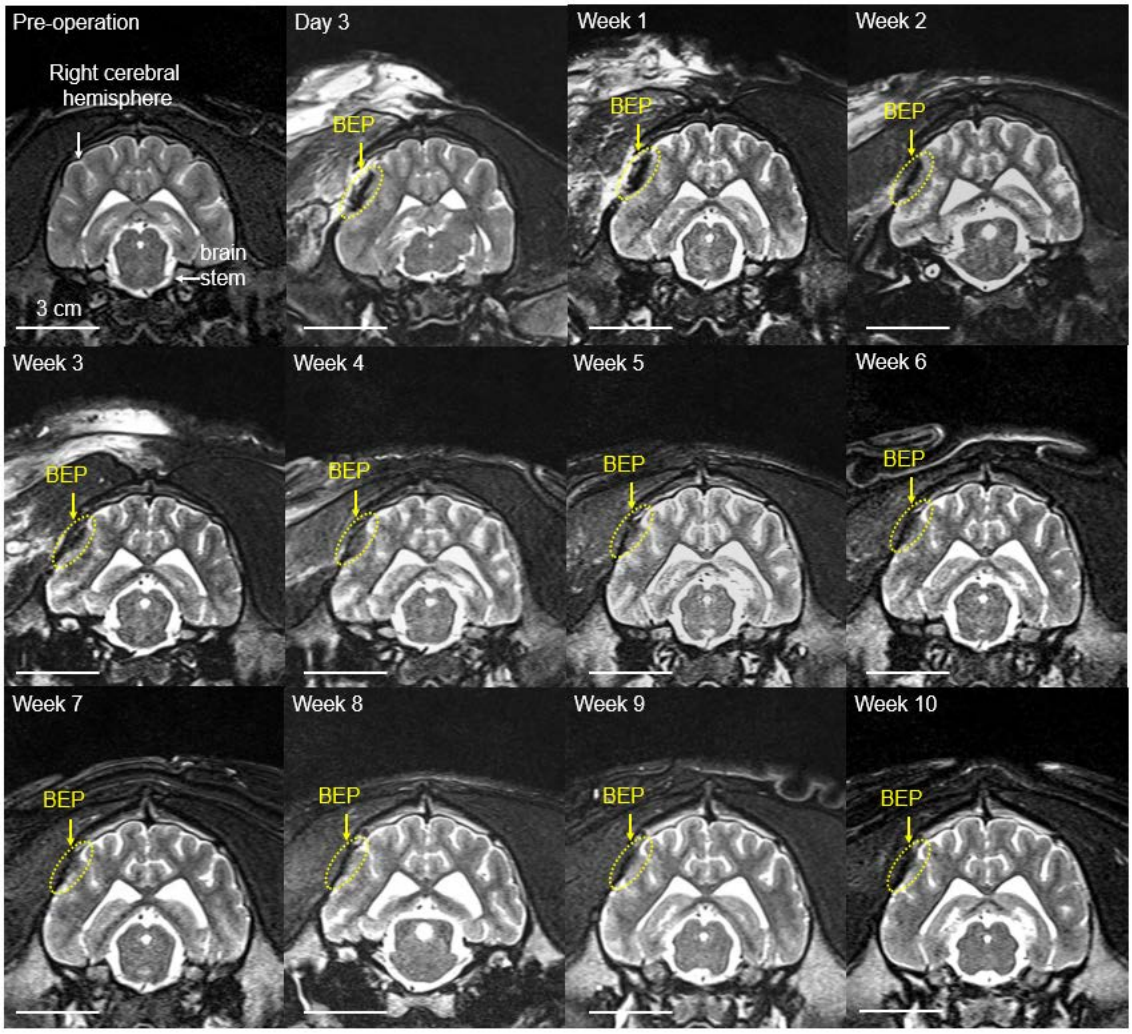

Supplementary Figure 11
MR images of the implanted BEP with the FION contrast agent at various time points. The device was implanted on the canine brain surface.

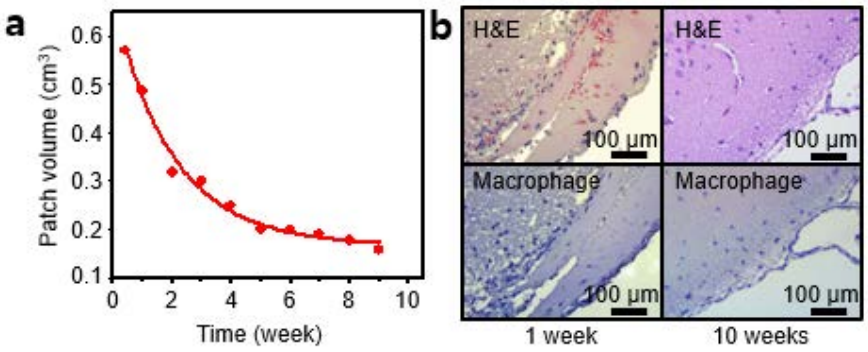

Supplementary Figure 12
(**a**) *In vivo* time-dependent patch volume change in the brain. (**b**) Histology images of tissues near the implantation site stained with hematoxylin and eosin (H&E; top) and macrophage antibody (bottom) after 1 week (left) and 10 weeks (right).

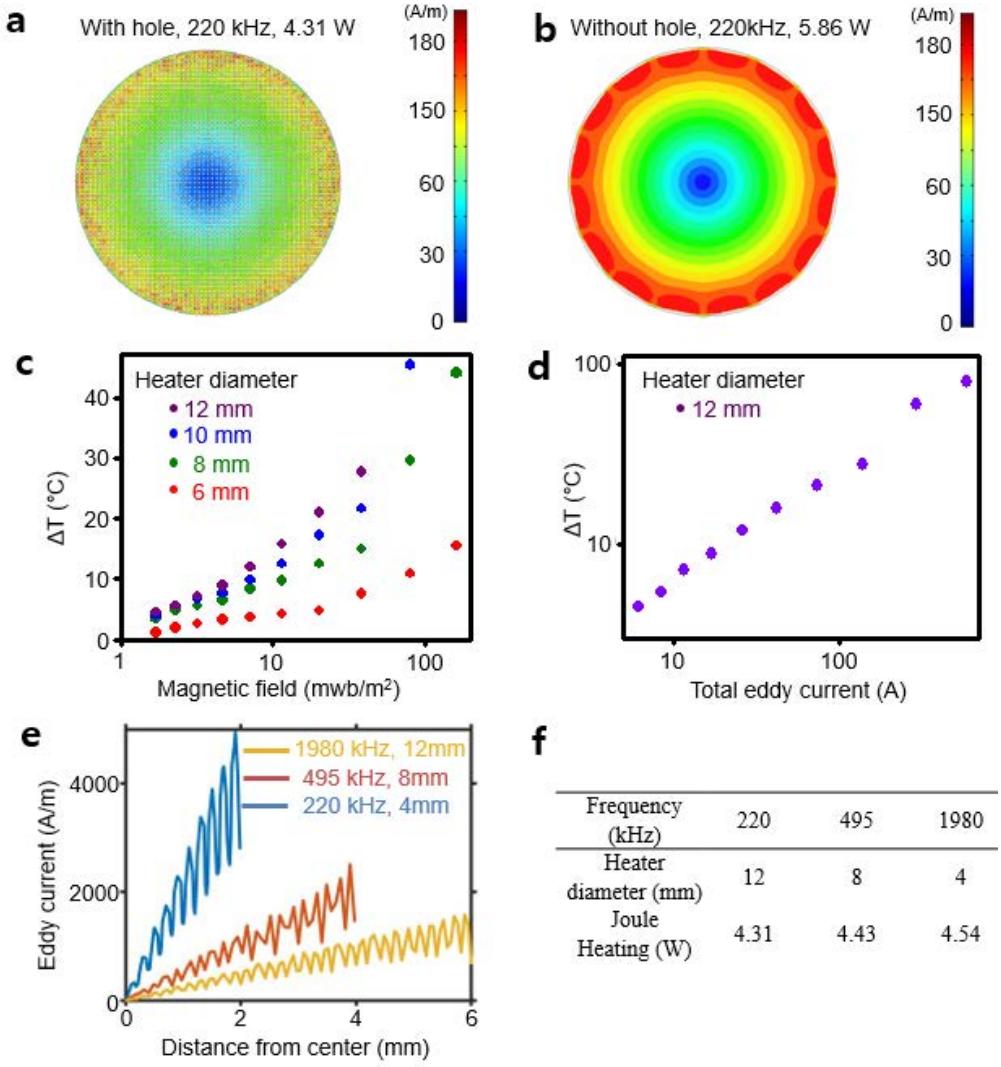

Frequency (kHz)	220	495	1980
Heater diameter (mm)	12	8	4
Joule Heating (W)	4.31	4.43	4.54

Supplementary Figure 13
Theoretical analysis and HFSS simulation of the wireless heater under different mild-thermic actuation conditions. 2-D Contour plot of the eddy current distribution of the BEP (**a**) with and (**b**) without the hole array under the optimized frequency. (**c**) Temperature increase by the wireless heater of various diameters as a function of the external magnetic field generated by the transmission coil. (**d**) Temperature increase by the wireless heater of 12 mm diameter as a function of the total eddy current. (**e**) 1-D eddy current from the center to the edge of the BEP with different frequencies and heater sizes. (**f**) Heat generation of the BEP with different frequencies and different heater sizes.

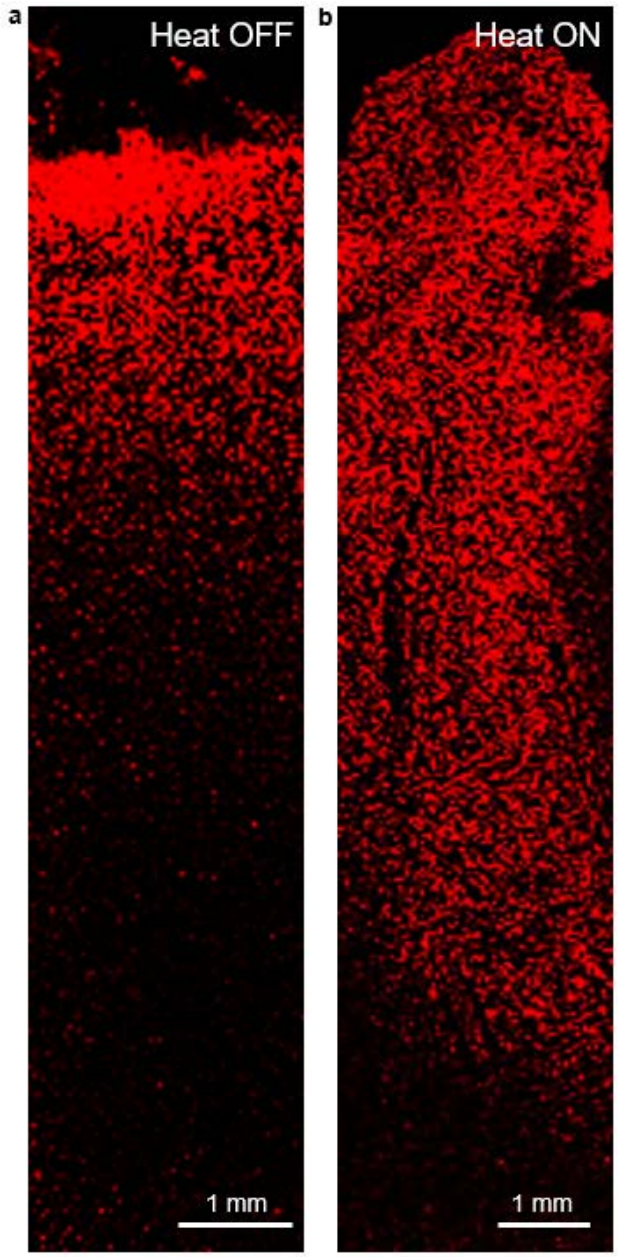

Supplementary Figure 14
Drug diffusion experiment over the extended period of time *ex vivo*. (**a**) DOX diffusion at 37 °C (left) and (**b**) 42 °C (right) for 48 h in the canine brain *ex vivo*.

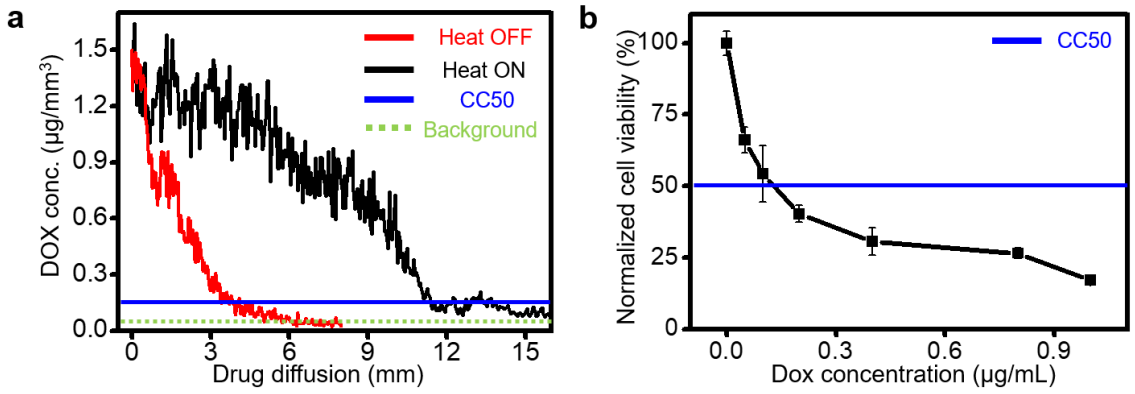

Supplementary Figure 15
DOX concentration measurement over the extended period of time *ex vivo* in the canine brain. (**a**) Distance dependent DOX concentration under the normal (37 °C; red) and mild-thermic actuation (42 °C; black) condition for 48 h in the canine brain *ex vivo*. (**b**) Cytotoxic concentration 50 (CC50) experiment of U87-MG in response to DOX.

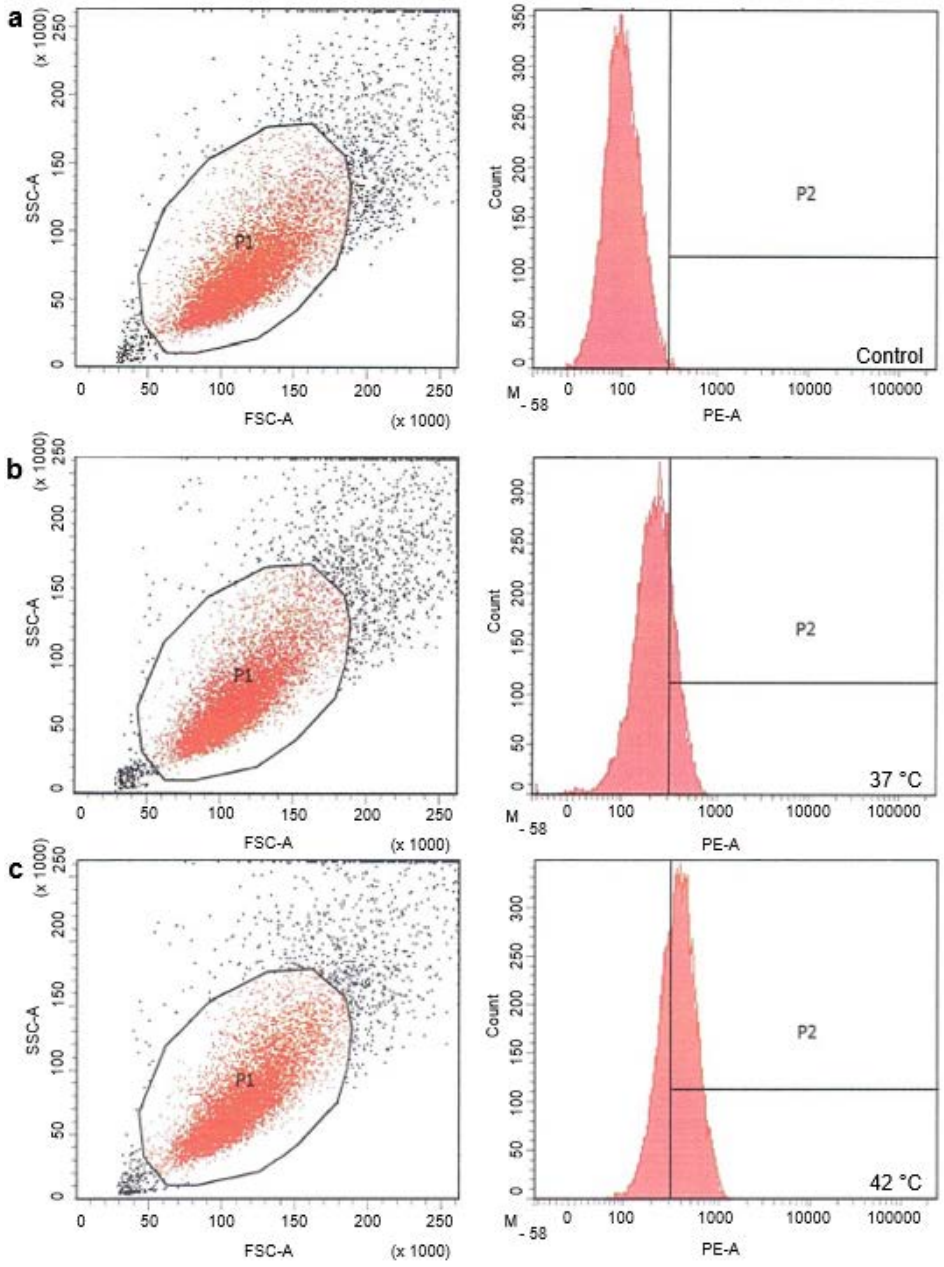

Supplementary Figure 16
Number of stained cells at different temperatures measured by flow cytometry. The left graphs show the tendency of Side-Scattered light Area (SSC-A) to Forward-Scattered light Area (FSC-A), and the right graphs show number of cells per Phycoerythrin area (PE-A). Cells are measured without DOX exposure for 1 hour a) negative control, and after exposure to the DOX solution for 1 hour at b) 37 and c) 42 °C.

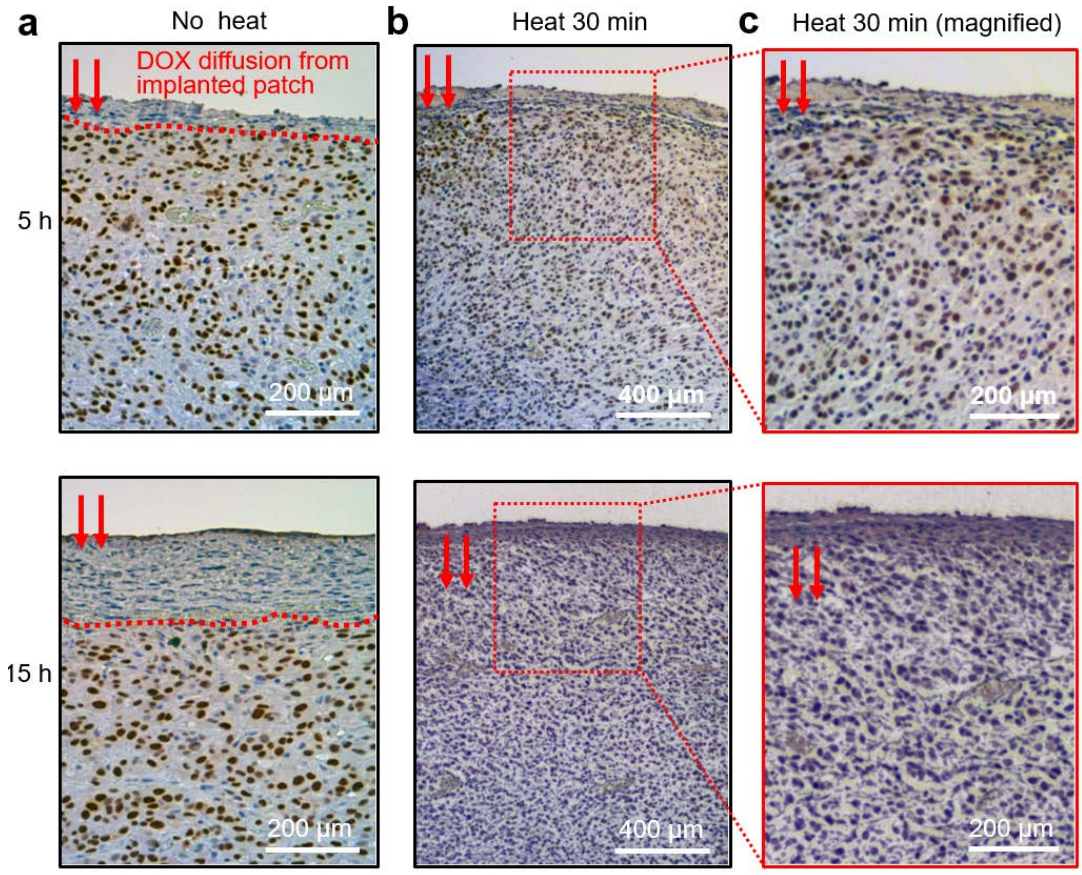

Supplementary Figure 17
Effect of DOX on survivin expression in U87-MG tumors at the indicated time-points. Survivin expression (**a**) without and (**b**) with heating ($\Delta T = 5$ °C). (**c**) Magnified image of (**b**).

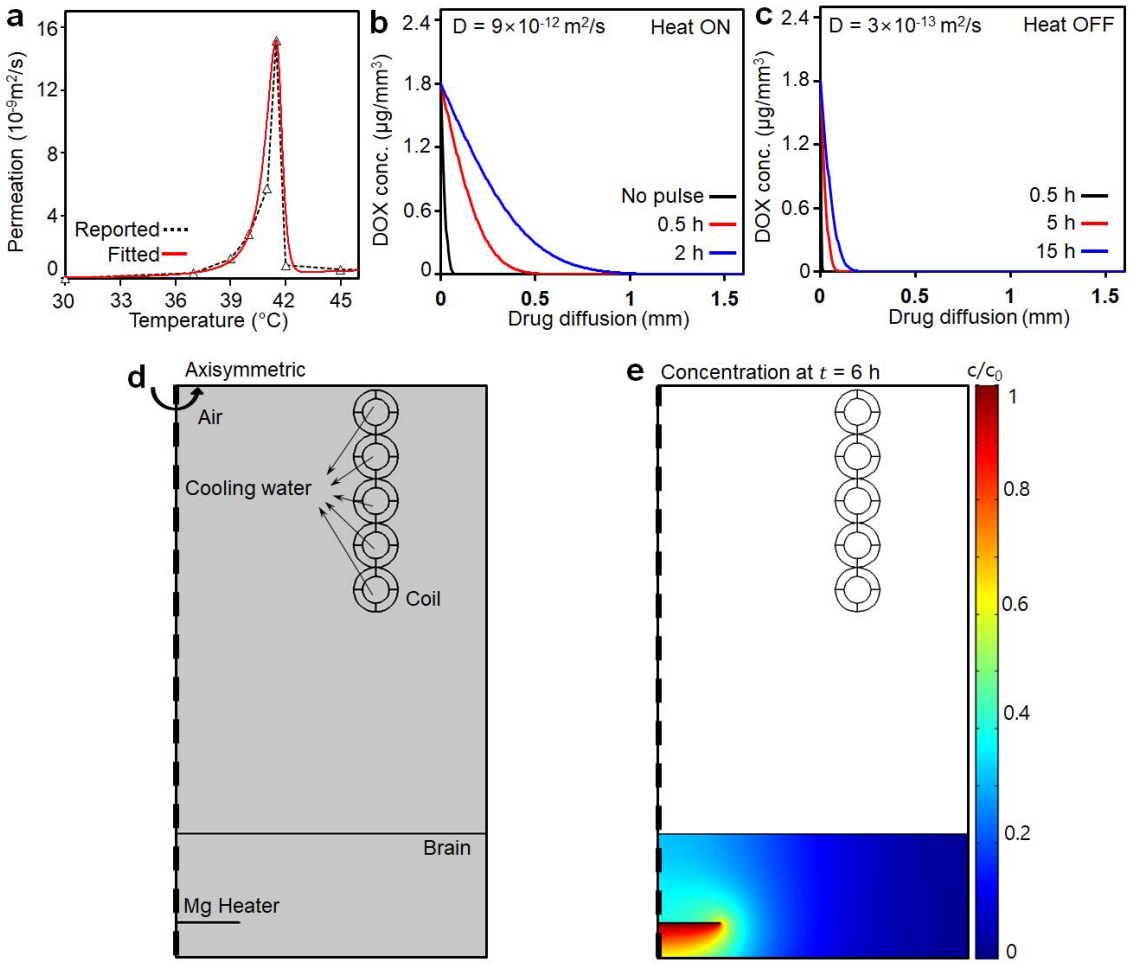

Supplementary Figure 18
Numerical simulations of drug diffusion in brain tissues as a function of temperature. (**a**) Plot of previously reported data and corresponding fitting of DOX permeation versus temperature in the lipid bilayer. Fitted plot of the DOX concentration as a function of distance from the interface between the BEP and brain, (**b**) without and (**c**) with heating. (**d**) Simulation input and (**e**) the normalized DOX profile in brain.

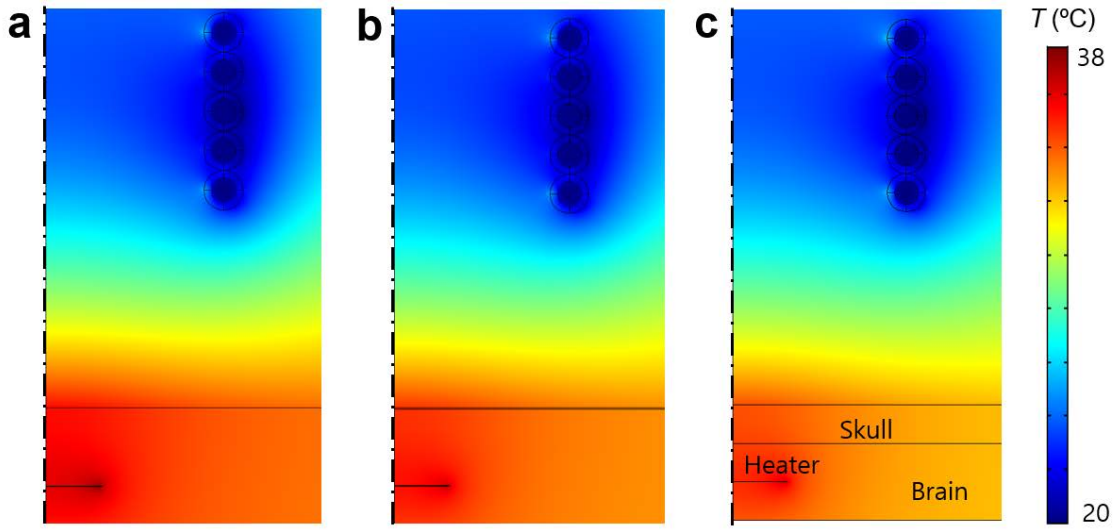

Supplementary Figure 19
The 3D FEM simulation results of contour plots depending on the different skull thickness. (**a**) No skull, (**b**) 0.15 mm thickness of skull (similar to mouse skull thickness), and (**c**) 5 mm thickness of skull (similar to human skull thickness).

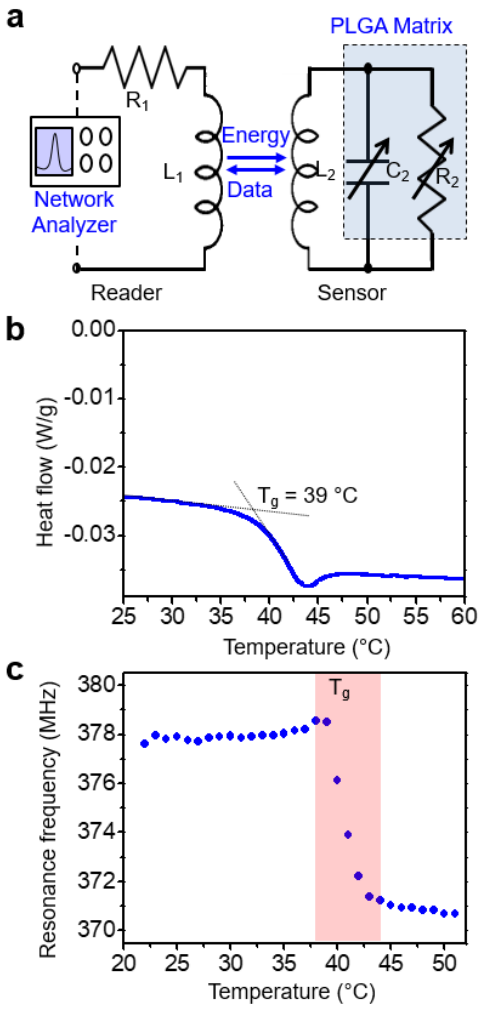

Supplementary Figure 20
Schematic illustration and characterization of the wireless temperature sensor.
(**a**) Circuit diagram of the wireless temperature sensor. (**b**) Differential scanning calorimetry curve around the glass transition temperature of poly(lactic-co-glycolic acid). (**c**) Resonance frequency change of the sensor as a function of temperature.

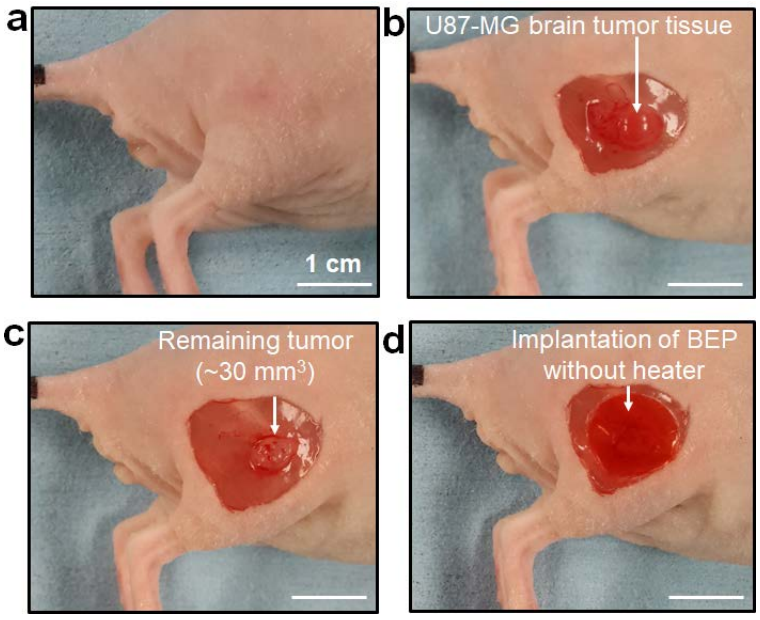

Supplementary Figure 21
Surgical process for the mouse brain tumor model.
(**a**) Optical camera image of an anesthetized mouse, (**b**) after resection of the mouse skin for brain tumor resection, (**c**) after the tumor resection surgery, and (**d**) after implantation of the BEP on the residual tumor.

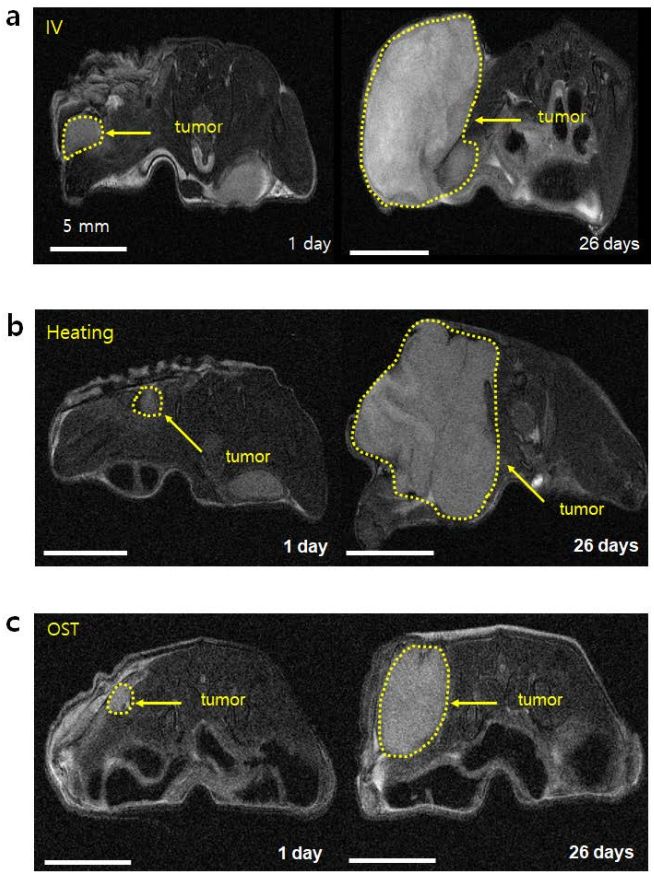

Supplementary Figure 22
MR images of the (**a**) IV group, (**b**) Heating group (no DOX), and (**c**) OST group (no heating) at the indicated time-points after surgery.

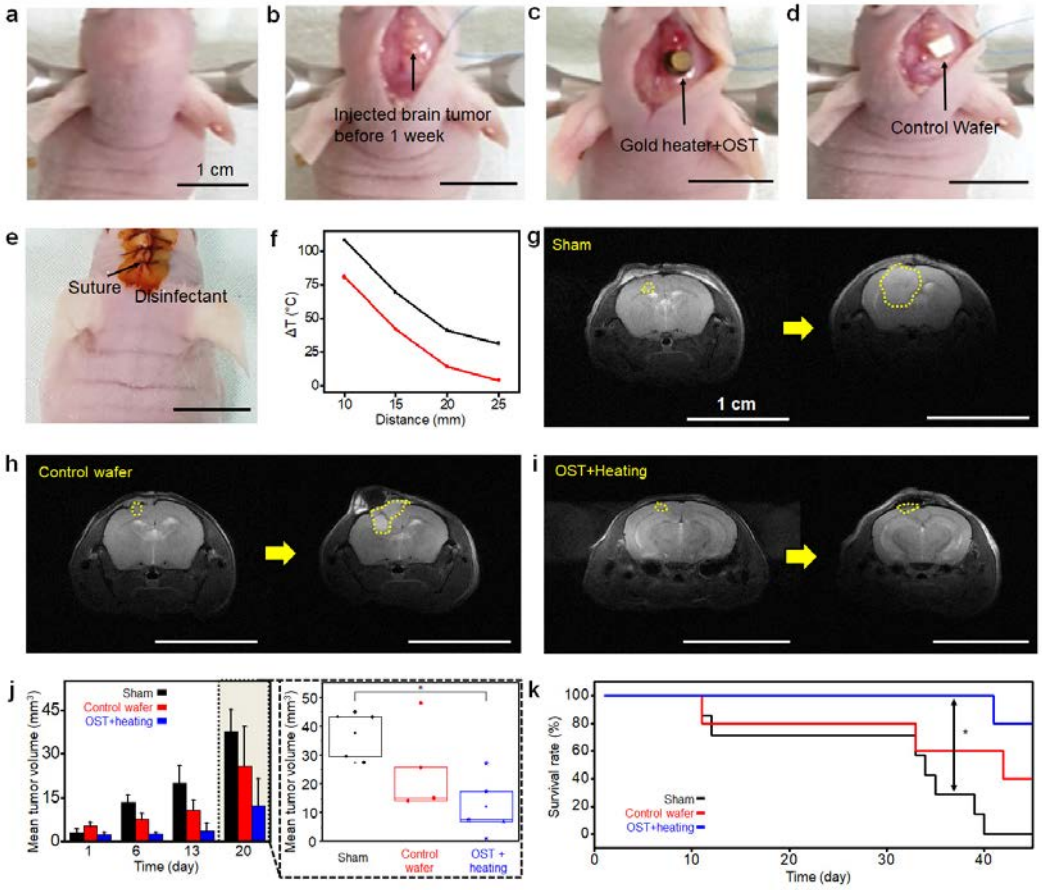

Supplementary Figure 23

Surgical process and therapeutic efficacy of the BEP in the mouse brain tumor model. (**a**) Fixation to the stereotaxic equipment and (**b**) incision of the skin of the mouse brain tumor model for neurosurgery. (**c**) Implantation of the miniaturized device composed of a gold heater and the OST patch and (**d**) a control wafer to the brain. (**e**) Skin suturing and disinfectant treatment. (**f**) Distance-dependent temperature changes of gold heater. Representative coronal T2-weighted MR images of the (**g**) 'Sham' group, (**h**) 'control wafer' group, and **i**. 'OST+heating' group at 1 day (left) and 2 weeks (right) after the surgery. (**j**) Time-dependent mean tumor volumes of the indicated groups (left) and box-and-whisker plots of tumor volumes at 20 days after the surgery (right). n = 7, 5, 5 for Sham, control wafer, and OST+heating group, respectively. Line: median Box: 25th to 75th percentiles, Whisker: min to max, *$p < 0.05$ by Man-Whitney U-test with Bonferroni correction. (**k**) Kaplan-Meier survival rate plots of the indicated group. *$p < 0.05$ by log-rank test with Bonferroni correction.

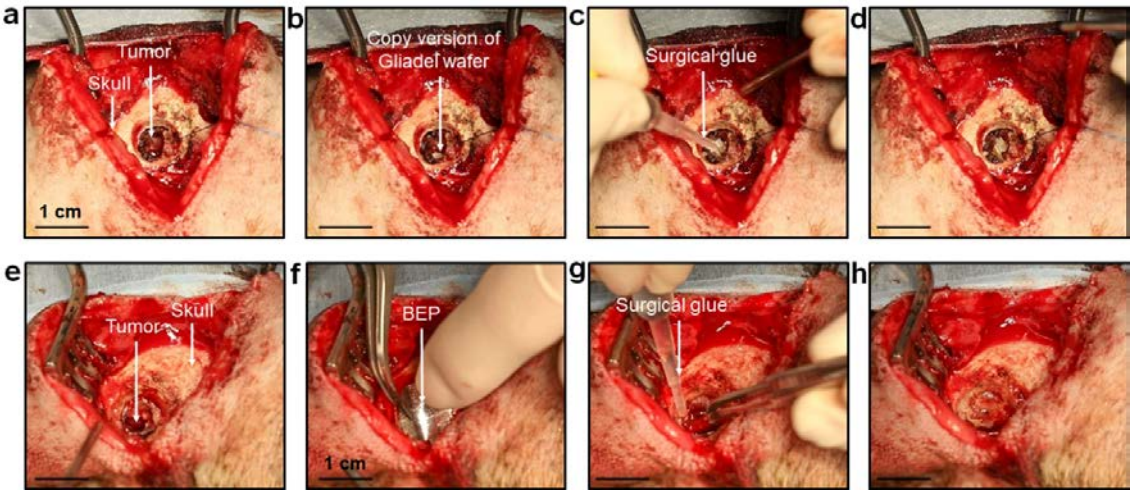

Supplementary Figure 24
Surgical process for tumor resection and BEP implantation in the canine brain model. Optical camera images show (**a**) before and (**b**) during implantation of the control wafer; (**c**) before and (**d**) after surgical glue injection; (**e**) before and (**f**) during BEP implantation; and (**g**) before and (**h**) after surgical glue injection.

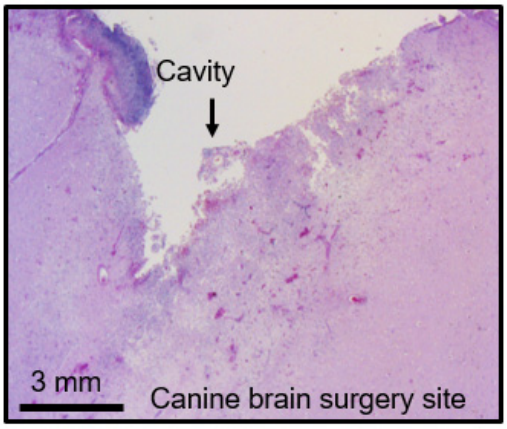

Supplementary Figure 25
Histology images of tissues (H&E) near the surgery site, which show the residual brain tumor infiltrated in the normal brain tissue.

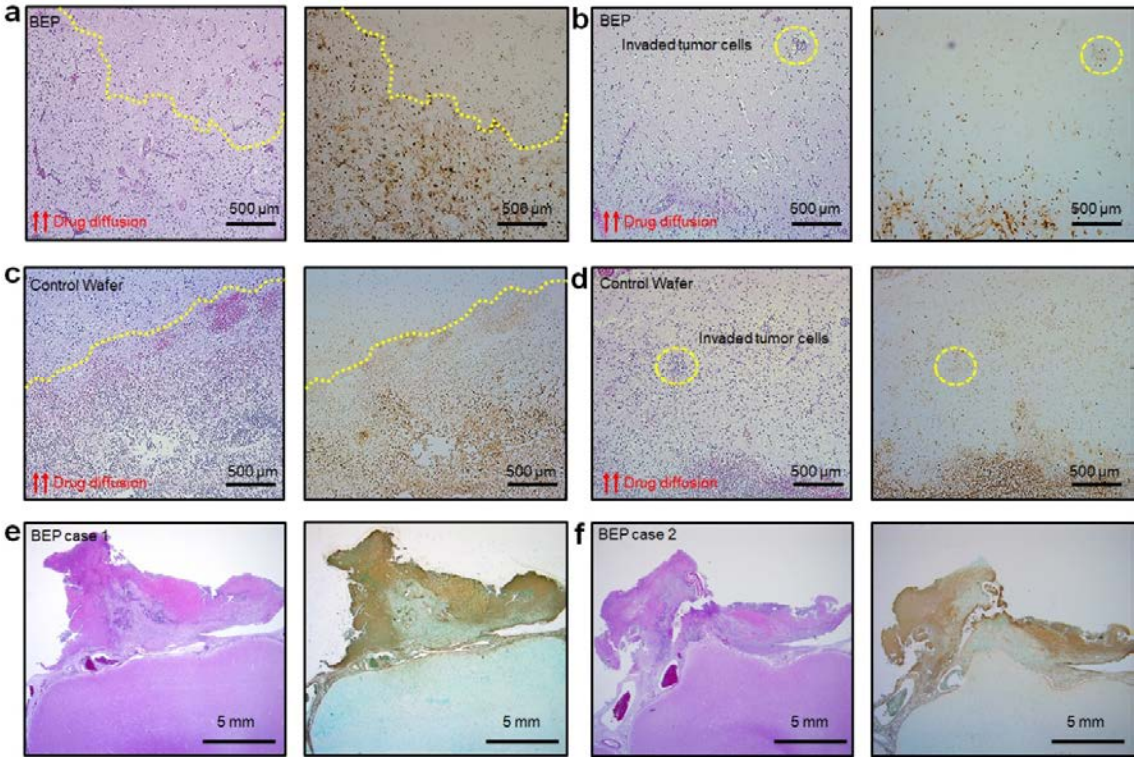

Supplementary Figure 26
Tumor specific death confirmed by H&E stain and TUNEL assay on same site in canine brain tumor model. (**a**) H&E stain (left) and TUNEL assay (right) of cavity which is treated by BEP after 2 days. (**b**) The dead invaded tumor cells with the BEP treatment. (**c**) H&E stain (left) and TUNEL assay (right) of tissues at the cavity after 2 days, which is treated by the control wafer. (**d**) The image of the untreated tumor cells in the control wafer case. (**e**), (**f**) H&E stained (left) and TUNEL assay (right) of the other site of the tumor cavity, which are treated by BEP after 1 week.

Supplementary Tables

	IV	Heating	OST	Control wafer
IV	-	-	-	-
Heating	NS	-	-	-
OST	$p = 0.0172$	NS	-	-
Control wafer	$p = 0.0025$	NS	NS	-
OST+Heating	$p = 0.0024$	$p = 0.0024$	$p = 0.019$	$p = 0.0048$

Supplementary Table 1
Statistical significance of the differences between the final tumor volumes in the indicated experimental groups, measured by 9.4 T magnetic resonance imaging. (IV, mice received an intravascular injection of DOX; Heating, mice received BEP and mild-thermic actuation, without DOX; OST, mice received BEP containing DOX; Control wafer, mice received Control wafer containing carmustine; OST+Heating, mice received BEP with DOX and mild-thermic actuation; NS, not significant, $p > 0.05$)
The comparison of final volume of all concerned mice in each group were evaluated by Mann-Whitney U test. The *p* value for individual tests was multiplied by the number of comparisons made (Bonferroni correction).

	IV	Heating	OST	Control wafer
IV	-	-	-	-
Heating	NS	-	-	-
OST	NS	$p = 0.0056$	-	-
Control wafer	$p = 0.0196$	$p = 0.0044$	NS	-
OST+Heating	$p = 0.0006$	$p = 0.0008$	$p = 0.036$	$p = 0.013$

Supplementary Table 2
Statistical significance of the differences between survival rates in the indicated experimental groups. IV, mice received an intravascular injection of doxorubicin (DOX); Heating, mice received bioresorbable electronic patch (BEP) and mild-thermic actuation, without DOX; OST, mice received BEP containing DOX; Control wafer, mice received Control wafer containing carmustine; OST+Heating, mice received BEP with DOX and mild-thermic actuation; NS, not significant, p value > 0.05)
The log-rank test was used to compare survival plot. The p value for individual tests was multiplied by the number of comparisons made (Bonferroni correction).

Elements	Thickness (μm)	Heat capacity (J kg^{-1} K^{-1})	Heat conductivity (W m^{-1} K^{-1})	Mass density (kg m^{-3})	Products
Cerebrospinal fluid	2000	4187	0.62	1000	
Top PLGA	5~100	1800	0.13	1300	Lactic acid
					Glycolic acid
Magnesium	3	1020	156	1738	Mg^{2+}
Bottom PLA	7	1800	0.13	1300	Lactic acid
Starch (77 % *w/w*)		1160	0.38	1500	Glucose
Glycerol (23 % *w/w*)		2413	0.29	1260	Glycerol
Drug reservoir	200	1449	0.36	1445	
Water (77 % *w/w*)		4187	0.62	1000	
Protein (9 % *w/w*)		1500	0.2	1450	
Fat (16% *w/w*)		2674	0.19	1000	
Brain tissue (White matter)	Infinite	3700	0.51	1030	
Doxorubicin	(1mg)				Doxorubicin

Supplementary Table 3
Thermophysical properties, thicknesses, and biodegradation products of the BEP layers.

	Symbol	Unit	Value
Relative permeability	μ_r	1	1
Relative permittivity	ϵ_r	1	850
Electric conductivity	σ	S m^{-1}	0.03
Heat capacity (constant pressure)	C_p	J kg^{-1} K^{-1}	1000
Density	ρ	Kg m^{-3}	1.9
Thermal conductivity	k	W m^{-1} K^{-1}	0.3

Supplementary Table 4
Electromagnetic properties of skull used in 3D FEM simulations.

Supplementary References

1. Mills, J. K. & Needham, D. Temperature triggered nanotechnology for chemotherapy: Rapid release from lysolipid temperature-sensitive liposomes. *NSTI-Nanotech* **2**, 5-8 (2006).
2. Gabriel, S., Lau, R. W. & Gabriel, C. The dielectric properties of biological tissues: III. Parametric models for the dielectric spectrum of tissues. *Phys. Med. Biol.* **41**, 2271-2293 (1996).
3. El-Brawany, M. A. *et al.* Measurement of thermal and ultrasonic properties of some biological tissues. *J. Med. Eng. Technol*. **33**, 249-256 (2009).
4. White, D. N., Curry, G. R. & Stevenson, R. J. The acoustic characteristics of the skull. *Ultrasound Med. Biol*. **4**, 225-252 (1978).
5. Krisht, A. F., Yoo, K., Arnautovic, K. I. & Al-Mefty, O. Cavernous sinus tumor model in the canine: A simulation model for cavernous sinus tumor surgery. *Neurosurgery* **56**, 1361-1366 (2005).
6. Whelan, H. T., Clanton, J. A., Wilson, R. E., Tulipan, N. B. Comparison of CT and MRI brain tumor imaging using a canine glioma model. *Pediatr. Neurol.* **4**, 279-283 (1988).
7. Johnston, M. The importance of lymphatics in cerebrospinal fluid transport. *Lymph. Res. Biol.* **1**, 41-45 (2003).
8. Jeon, D. *et al.* A cell-free extract from human adipose stem cells protects mice against epilepsy. *Epilepsia* **52**, 1617-1626 (2011).
9. Lee, S.-T. *et al.* Slowed progression in models of huntington disease by adipose stem cell transplantation. *Ann. Neurol.* **66**, 671-681 (2009).
10. Lee, S.-T. *et al.* Inhibition of miR-203 reduces spontaneous recurrent seizures in mice. *Mol. Neurobiol.* **54**, 3300-3308 (2017).